ornl

ORNL-6067

OAK RIDGE NATIONAL LABORATORY

MARTIN MARIETTA

Initial Development of Nickel and Nickel-Iron Aluminides for Structural Uses

C. T. Liu
W. Jemian
H. Inouye
J. V. Cathcart
S. A. David
J. A. Horton
M. L. Santella

OPERATED BY
MARTIN MARIETTA ENERGY SYSTEMS, INC.
FOR THE UNITED STATES
DEPARTMENT OF ENERGY

Printed in the United States of America. Available from
National Technical Information Service
U.S. Department of Commerce
5285 Port Royal Road, Springfield, Virginia 22161
NTIS price codes—Printed Copy: A04 Microfiche A01

ORNL-6067

METALS AND CERAMICS DIVISION

INITIAL DEVELOPMENT OF NICKEL AND NICKEL-IRON ALUMINIDES FOR STRUCTURAL USES

C. T. Liu, W. Jemian, H. Inouye, J. V. Cathcart,
S. A. David, J. A. Horton, and M. L. Santella

Date Published - August 1984

Prepared for
Office of Fossil Energy
and
Office of Conservation

Prepared by the
OAK RIDGE NATIONAL LABORATORY
Oak Ridge, Tennessee 37831
Operated by
MARTIN MARIETTA ENERGY SYSTEMS, INC.
for the
U.S. DEPARTMENT OF ENERGY
under Contract No. DE-AC05-840R21400

CONTENTS

ORNL-6067

INITIAL DEVELOPMENT OF NICKEL AND NICKEL-IRON ALUMINIDES FOR STRUCTURAL USES*

C. T. Liu, W. A. Jemian,† H. Inouye, J. V. Cathcart,
S. A. David, J. A. Horton, and M. L. Santella

ABSTRACT

Initial development of ductile nickel and nickel-iron aluminides has concentrated on boron-doped Ni_3Al alloyed with iron and other elements. The aluminide can dissolve no more than 15 at. % Fe, beyond which formation of both transformed *B*2 phase (β') and disordered fcc phase (γ) is observed. Nickel-iron aluminides were tensile tested as a function of temperature. Iron additions strengthen Ni_3Al effectively at temperatures to 850°C. The yield stress of the nickel-iron aluminides increases with test temperature and reaches a maximum around 650°C. The high-temperature strength of the aluminides can be further improved by alloying with less than 2 at. % Hf. Hafnium-modified aluminides are stronger than commercial superalloys, including some cast superalloys.

Hot corrosion behavior of nickel-iron aluminides was determined in quartz capsules and in a circulating loop system containing a supply of $CaSO_4$ at temperatures to 871°C (1600°F). The combined results from these tests showed the dependence of sulfidation on oxygen partial pressure and verified that the sulfidation attack of aluminides in capsule tests was caused by oxygen depletion in a closed system with a limited supply of oxygen. The aluminides exhibited superior oxidation resistance in air at temperatures to 1100°C.

The ductile aluminides are prone to hot cracking during welding. However, they can be electron beam welded successfully under closely controlled conditions. Boron content and welding speed affect the weldability of the aluminides.

---

*Research sponsored jointly by the U.S. Department of Energy (DOE/FE AA 15 10 10 0, AR&TD Fossil Energy Materials Program, Work Breakdown Structure Element ORNL-3.1) and the Energy Conservation and Utilization Technologies (ECUT) Program under contract DE-AC05-840R21400 with the Martin Marietta Energy Systems, Inc.

†Mechanical Engineering and Materials Engineering Department, Auburn University, Auburn, Alabama.

INTRODUCTION

Current structural alloys, such as austenitic stainless steels and superalloys, generally do not have the combination of strength, ductility, and corrosion resistance required for structural uses in advanced heat engines and coal conversion and utilization systems. Coating materials such as FeCrAl, on the other hand, possess good corrosion resistance but lack adequate strength at elevated temperatures. There is thus a pressing need for the development of new improved alloys for structural applications in hostile environments at elevated temperatures. The objective of this task is to design and test materials that possess good mechanical properties and resist hot corrosion at high temperatures. Aluminides based on Ni_3Al, Fe_3Al, NiAl, and FeAl have been chosen for development of new materials with the required properties.

Ordered intermetallic compounds based on nickel and iron aluminides have unique properties that make them attractive for structural applications at elevated temperatures.[1-4] These aluminides are typically resistant to oxidation as a result of their ability to form protective aluminum oxide scales. The strong tendency for long-range order in these alloys reduces atomic mobility at elevated temperatures and results in good structural stability and resistance to high-temperature deformation by diffusion-controlled processes. Because the aluminides do not contain chromium and cobalt, present in many current structural materials, successful development of structural aluminides could substantially reduce the nation's dependence on these critical strategic materials.

The major difficulty with using aluminides as engineering materials is their low ductility and tendency for brittle fracture. This brittleness effectively precludes fabrication into most structural components. However, recent studies[5-9] have demonstrated that the ductility and fabricability of ordered intermetallic alloys can be dramatically improved by microalloying and macroalloying processes. Macroalloying involves adding major concentrations (several percent or more) of alloying elements to control ordered crystal structure and bulk properties. Microalloying is the addition of minor concentrations (usually parts-per-million range) of

elements to control grain-boundary composition or structure. These studies have laid the groundwork for the development of new structural materials based on ordered intermetallic alloys including aluminides.

Initial development of nickel-iron aluminides included three subtasks. The first one is the basic alloy development, which attempts to improve the mechanical and metallurgical properties of Ni_3Al by alloying with iron and other elements. Polycrystalline Ni_3Al is very brittle because of grain boundary weakness.[9-10] However, in work funded internally by ORNL and by the DOE Basic Energy Sciences Program we found that the ductility and fabricability of Ni_3Al can be dramatically improved through alloying with a few hundred parts per million of boron, which strongly segregates to the grain boundaries[7-8] and improves grain boundary cohesion. The development work in this subtask includes alloy preparation and fabrication, determination of microstructure and phase relationships, characterization of tensile properties, and study of oxidation behavior.

The second subtask is to determine the corrosion behavior of nickel-iron aluminides in sulfidizing-oxidizing environments. The goal of this study is to provide input into the development of sulfidation-resistant aluminides suitable for use in advanced coal conversion systems. The third subtask is to determine the weldability of the nickel-iron aluminides because an important area in the development of new alloys is the ease with which they can be joined or welded. Preliminary studies indicate that the aluminides are quite prone to hot cracking during welding thermal cycles. The primary goal of this subtask is to improve the weldability of selected aluminides through control of welding parameters and alloy composition.

The development of nickel and nickel-iron aluminides is jointly supported by the Advanced Research and Technology Development (AR&TD) Fossil Energy Materials Program and the Energy Conversion and Utilization Technologies (ECUT) Program of the U.S. Department of Energy (DOE). The ECUT Program focuses on development of nickel aluminides based on Ni_3Al as a new class of structural materials for use in high-efficiency advanced heat engines (e.g., Stirling engines, adiabatic diesel engines) and high-temperature heat recovery systems (e.g., heat exchangers). The

Fossil Energy Materials Program concentrates on the development of nickel-iron aluminides as structural materials for hot components exposed to severe environments in coal gasifiers, coal liquefaction systems, fluidized-bed combustors, and fuel cells.

BASIC ALLOY DEVELOPMENT

ALLOY PREPARATION AND FABRICATION

Three series of aluminide alloys were prepared for the basic alloy development. The first series of aluminides, having the designations and compositions listed in Table 1, was based on Ni_3Al alloyed with iron. All the aluminides were doped with 0.05 wt % B to improve ductility. The function of the added iron is to (1) strengthen Ni_3Al by solid-solution hardening and (2) lower the nickel content to reduce material cost and improve corrosion resistance. A maximum of 20 at. % Fe (20.9 wt %) was added to replace both nickel and aluminum atoms in Ni_3Al (Table 1).

The second series of aluminides (Table 2) was based on Ni_3Al alloyed with other elements including Hf, Zr, Ti, Mn, Nb, and Ta to improve metallurgical and mechanical properties, particularly at elevated temperatures.

Table 1. Composition of nickel aluminides with iron additions

Alloy	Content (at. %)[a]		Content (wt. %)[a]		Alloy fabrication results
	Al	Fe	Al	Fe	
IC-15	24	0[b]	12.7	0[b]	Sheet fabricated
IC-37	24.5	1	13.0	1.1	Alloy cracked badly during sheet fabrication
IC-45	24	1	12.7	1.1	Cracked during fabrication
IC-38	24	2	12.7	2.2	Fabricated with difficulty
IC-64	22	6	11.5	6.5	Sheet fabricated
IC-46	20	10	10.4	10.7	Sheet fabricated
IC-47	20	15	10.4	16.1	Sheet fabricated
IC-39	17.5	15	9.0	15.9	Sheet fabricated
IC-65	15	20	7.6	20.9	Sheet fabricated

[a]0.2 at. % or 0.05 wt. % B, balance nickel.

[b]Base alloy.

Table 2. Composition of nickel aluminides with alloy additions other than iron

Alloy	Content (at. %)[a]		Alloy	Content (at. %)[a]	
	Al	Other		Al	Other
IC-15	24		IC-74	23.5	0.5 Ti
IC-71	23.75	0.25 Hf	IC-44	23.5	1.0 Ti
IC-50	23.5	0.5 Hf	IC-43	22.5	2.0 Ti
IC-49	24.0	0.5 Hf	IC-29	20.0	4.0 Ti
IC-72	23.0	1.0 Hf	IC-73	23.5	0.5 Zr
IC-76	22.5	1.5 Hf	IC-53	23.0	1.0 Mn
IC-77	22.0	2.0 Hf	IC-30	20.0	4.0 Nb
IC-78	21.0	3.0 Hf	IC-31	20.0	4.0 Ta

[a]0.2 at. % B, balance nickel.

The third series was based on nickel-iron aluminides containing about 10 at. % Fe. The alloy compositions in Table 3 were based on the results obtained from the first and second series. Up to 0.2 wt. % (~0.8 at. %) C was added for particle strengthening through precipitation of carbides.

Aluminides with compositions listed in Tables 1 through 3 were prepared by arc melting and drop-casting from pure metals, pyrolytic carbon, and a master alloy of Ni—4 wt % B. The drop-casting technique was used to refine the ingot grain structure and reduce compositional segregation during solidification. Preliminary study indicated that the aluminides could be best fabricated by cold rolling rather than hot fabrication. Consequently, alloy ingots (25 × 57—125 × 6—10 mm), homogenized for 5 h at 1000°C, were fabricated into sheet stock by repeated rolling at room temperature with intermediate anneals at 1000 to 1050°C. The cold work, initially a 10 to 15% reduction of thickness, was gradually increased to 25 to 30% between successive intermediate anneals.

The effect of iron on aluminide fabricability is shown in Table 1. The aluminides containing 2 at. % Fe or less cracked badly during cold rolling, indicating that a small amount of iron is detrimental to the fabricability of Ni_3Al. On the other hand, the aluminides with 6 to 15 at. % Fe were readily fabricated into 0.08-mm-thick sheets. The cold fabricability of IC-46 (Ni—20 Al—10 Fe—0.2 B, at. %) is better than that

Table 3. Compositions of nickel-iron aluminides with alloy additions

Alloy	Content (wt %), balance nickel							Content (at. %), balance nickel						
	Fe	Al	Mn	Ti	Hf	B	Other	Fe	Al	Mn	Ti	Hf	B	Other
IC-25	10.7	9.8	0.5	0.5		0.05		10.0	19	0.5	0.5		0.2	
IC-26	10.9	11.3	0.5	0.5		0.05		10.0	21.5	0.5	0.5		0.2	
IC-103	10.7	9.8	0.5	0.5		0.02		10.0	19	0.5	0.5		0.08	
IC-14	10.7	10.1	1.0	0.5		0.05		10.0	19.5	1.0	0.5		0.2	
IC-61	10.4	10.3	0.5	0.5		0.01	1.33 Nb	9.8	20	0.5			0.04	0.75 Nb
IC-17	10.4	10.0	0.5	0.5		0.05	1.33 Nb	9.8	19.5	0.5	0.5		0.2	0.7 Nb
IC-63	10.6	10.2	0.5		1.7	0.05	0.04 C	10.0	20	0.5		0.5	0.2	0.16 C
IC-68	9.5	10.1	0.5		1.7	0.05	1.7 Ta 0.04 C	9.1	20	0.5		0.5	0.2	0.5 Ta 0.16 C
IC-69	9.6	10.2	0.5		1.7	0.05	0.9 Nb 0.04 C	9.1	20	0.5		0.5	0.2	0.5 Nb 0.16 C
IC-101	9.4	9.8			3.3	0.02		9.0	19.5			1	0.08	
IC-40	10.8	10.4				0.05	5.0 Cr	10	20				0.2	5 Cr
IC-32	10.6	9.8	0.5	0.9		0.05	0.1 C	10.0	19.0	0.5	0.9		0.2	0.5 C
IC-33	10.6	9.7	0.5	1.1		0.05	0.2 C	10.0	19.0	0.5	1.1		0.2	0.9 C

of IC-15 (Ni—24 Al—0.2 B), which contains no iron. Sheet fabrication became increasingly difficult with the iron content above 15%. The aluminide containing 20% Fe showed some surface and end cracking and was difficult to roll into sheet.

The aluminides (except IC-30 and -31, which contain 4 at. % Nb and Ta, respectively) in Tables 2 and 3 were fabricated into sheet materials. A small amount (<2 at. %) of Hf, Zr, and Mn improved the cold fabricability of Ni_3Al. Sulfur, a trace impurity, has a strong tendency to segregate and embrittle grain boundaries in Ni_3Al (ref. 8). The beneficial effect of Hf, Zr, and Mn is believed to come from the removal of sulfur from the grain boundaries by precipitation of sulfides.[11] The nickel-iron aluminides IC-32 and -33, containing 0.1 and 0.2 wt % C, respectively, were also readily fabricated into sheets without difficulty.

Chemical compositions of selected aluminides were determined by volumetric and gravimetric analyses of major elements, spark source mass spectroscopy of trace impurities, and vacuum fusion and Leco carbon analyses of interstitial elements (such as O, N, and H). The boron concentrations agreed very well with nominal compositions, indicating no major difficulty in controlling the boron dopants in the aluminides. The major elements are also in good agreement with the nominal compositions. This close agreement was expected because ingot weights did not change appreciably during arc melting. Trace impurities and interstitial contents both were very low in the aluminides. For example, the sulfur level was less than 1 to 3 ppm, and the total oxygen and carbon contents were less than 150 ppm by weight.

MICROSTRUCTURE AND PHASE RELATIONSHIPS

Microstructures and phase relationships in the aluminides were studied by both optical and transmission electron microscopy. Figure 1 shows the effect of iron additions on the microstructure of Ni_3Al. All specimens were recrystallized for 1 h at 1050°C. The aluminides containing up to 10 at. % Fe exhibit a single-phase structure. Second-phase particles are clearly observed in Ni—20 Al—15 Fe (IC-47) but not in Ni—17.5 Al—15 Fe (IC-39), even though both aluminides contain 15 at. % Fe.

Y-195272

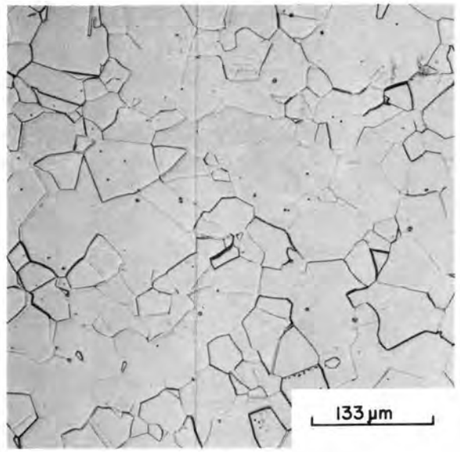

(*a*)

Y-195332

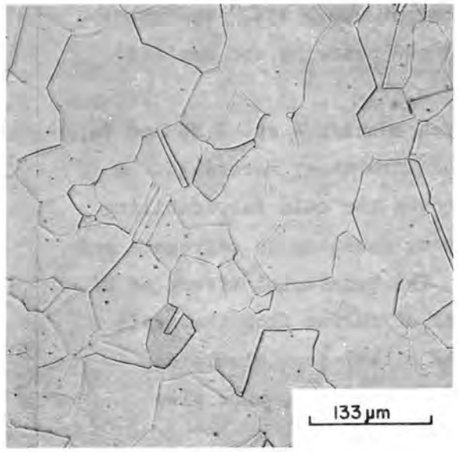

(*b*)

Y-189830

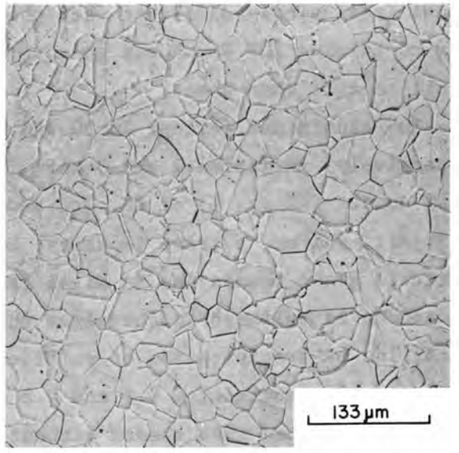

(*c*)

Y-189831

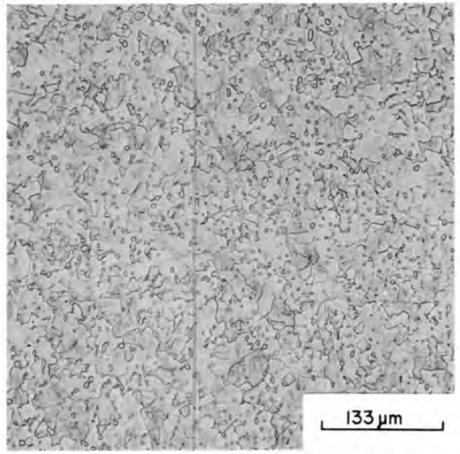

(*d*)

Y-195324

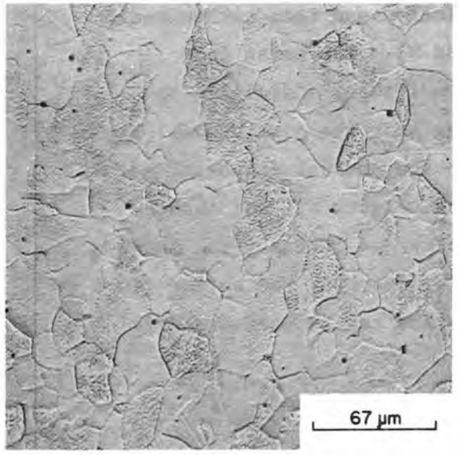

(*e*)

Y-195327

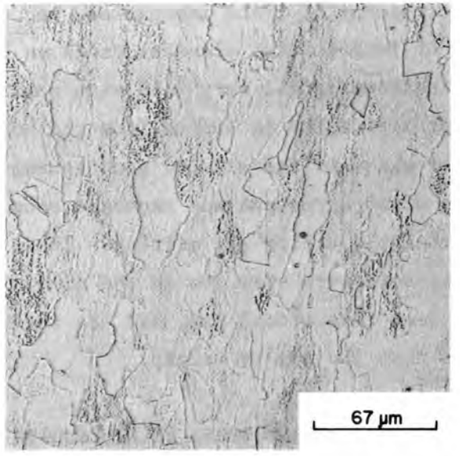

(*f*)

Fig. 1. Optical microstructures of Ni_3Al with iron additions. Etched with 20 H_2O, 20 HNO_3, 10 HF, 20 H_3PO_4, 10 acetic acid, and 10 HCl (parts by volume). (*a*) IC-15, Ni–24 Al–0.2 B (at. %). (*b*) IC-64, Ni–22 Al–6 Fe–0.2 B. (*c*) IC-46, Ni–20 Al–10 Fe–0.2 B. (*d*) IC-47, Ni–20 Al–15 Fe–0.2 B. (*e*) IC-39, Ni–17.5 Al–15 Fe–0.2 B. (*f*) IC-65, Ni–15 Al–20 Fe–0.2 B.

This observation suggests that the aluminum-to-nickel ratio affects the iron solubility and the formation of second phases. It was difficult to reveal the grain structure in IC-39 and IC-65 (Ni—15 Al—20 Fe) [Fig. 1(*e*) and (*f*)] by etching or to prevent the staining of the specimens by the etching solution.

Transmission electron microscopy (TEM) studies were performed on aluminides containing 10 to 20 at. % Fe. All specimens were annealed for 1 h at 1050°C and tensile tested at room temperature or 600°C. Specimens for TEM were spark cut from the grip ends of sheet tensile specimens. The aluminide with 10 at. % Fe (IC-46, 70 Ni—20 Al—10 Fe) was single phase with the ordered $L1_2$ structure with no observed precipitation in the grains or on the grain boundaries, indicating that the iron had remained in solution. No antiphase boundaries were observed, suggesting that iron additions have little effect on ordering. An example of the featureless microstructure is shown in Fig. 2.

Two aluminides with 15 at. % Fe, IC-39 and -47, were studied in detail by TEM. The IC-39 specimen, which was prepared from the shoulder of the tensile specimen tested at 600°C, contained a well developed dislocation cell structure (Fig. 3) and a complex cellular structure (Fig. 4). Figure 4 is a TEM taken deliberately out of focus, showing ordered regions as dark areas and disordered regions as bright areas (preferentially etched). The cellular structure consisted of small islands of ordered $L1_2$ material surrounded by a web of disordered gamma material. The ordered islands had the same orientation as the ordered matrix grains that surrounded the island-web region. The IC-47 specimen, which was prepared from the shoulder of the tensile specimen tested at room temperature, had a relatively low dislocation density and contained scattered regions of cellular structures (Fig. 5) and martensitic particles (Fig. 6). The crystal structure of the martensitic particles in Fig. 6 has not been positively identified, but it is not the regular $L1_2$ or $B2$ (ordered bcc structure). Instead, the structure is similar to the tetragonal and orthorhombic distortions of either the $L1_2$ or $B2$, which are known to occur in rapidly solidified nickel aluminides with a variety of aluminum contents.[12] The composition of the martensitic particles was found by energy-dispersive spectroscopic (EDS) analysis to be enriched in aluminum by

YE-12787

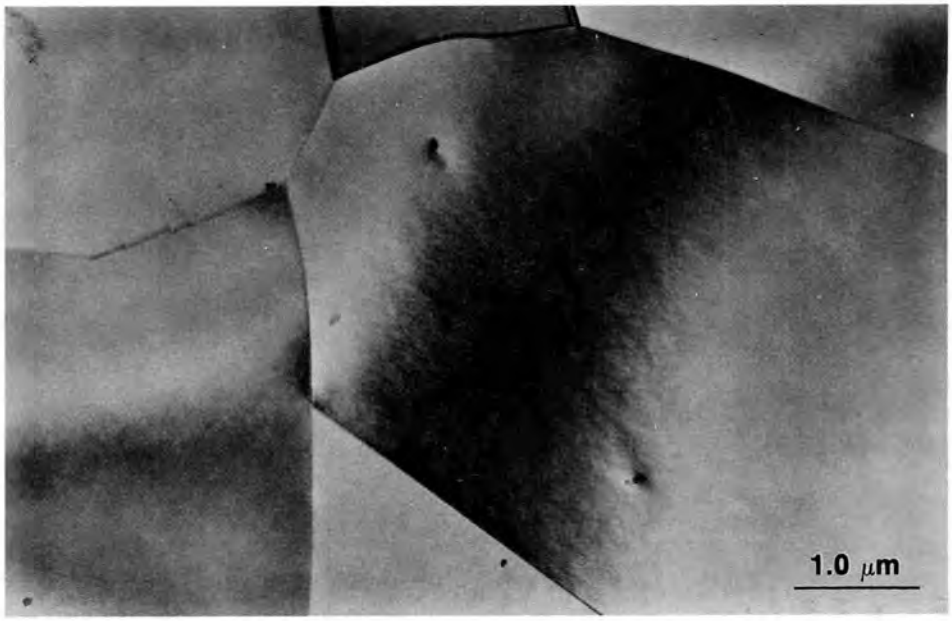

Fig. 2. Transmission electron micrograph of IC-46 (Ni—20 Al—10 Fe—0.2 B, at. %) recrystallized for 1 h at 1050°C, showing single-phase grain structure.

YE-12788

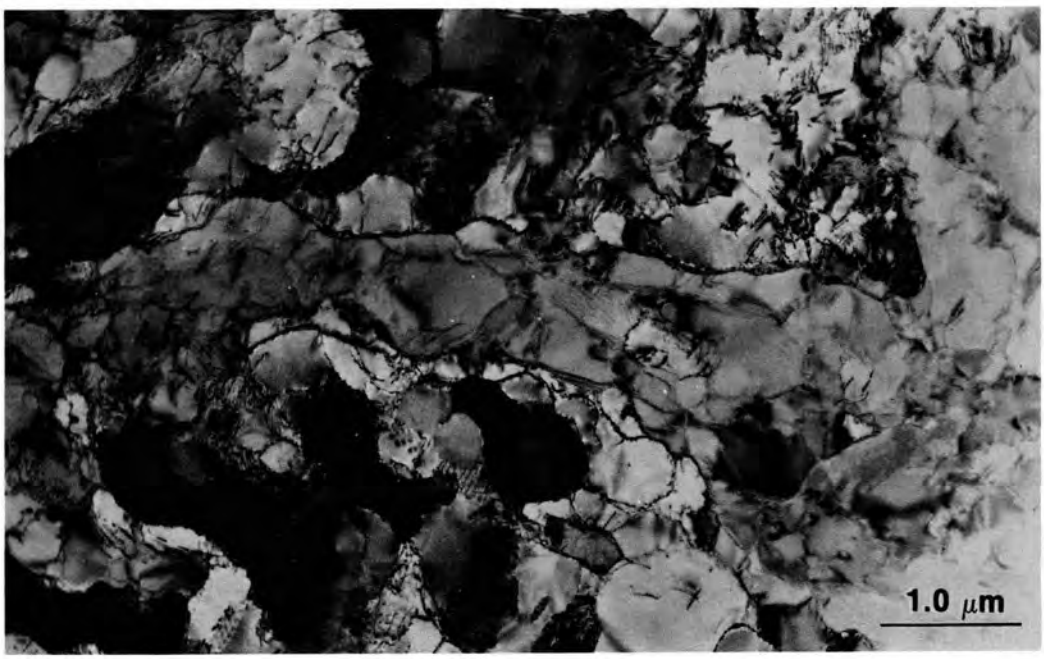

Fig. 3. Transmission electron micrograph of IC-39 (Ni—17.5 Al—15 Fe—0.2 B, at. %) showing a well-developed dislocation cell structure.

YE-12785

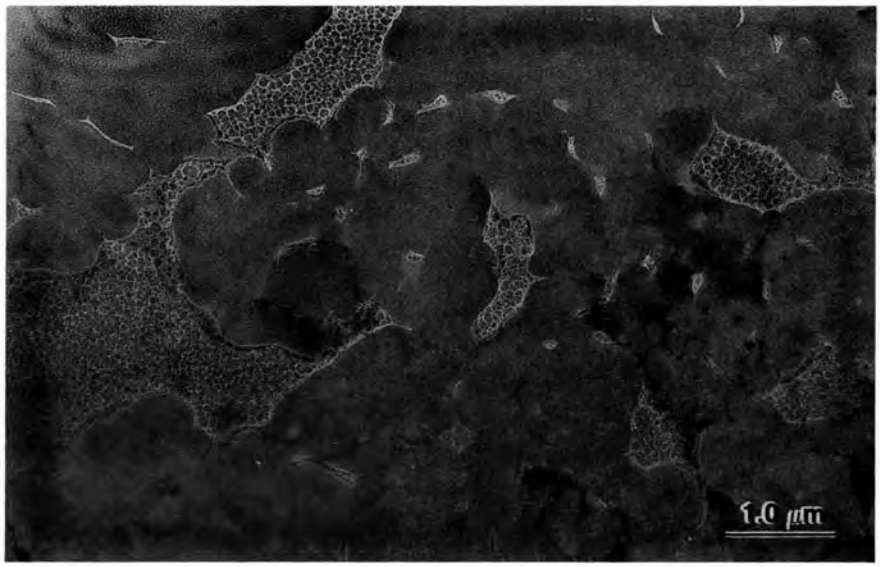

Fig. 4. Dark-field transmission electron micrograph (deliberately out of focus) of IC-39 (Ni—17.5 Al—15 Fe—0.2 B, at. %) showing the cellular structure of small islands of ordered $L1_2$ material surrounded by a web of disordered gamma material (preferentially etched).

YE-12786

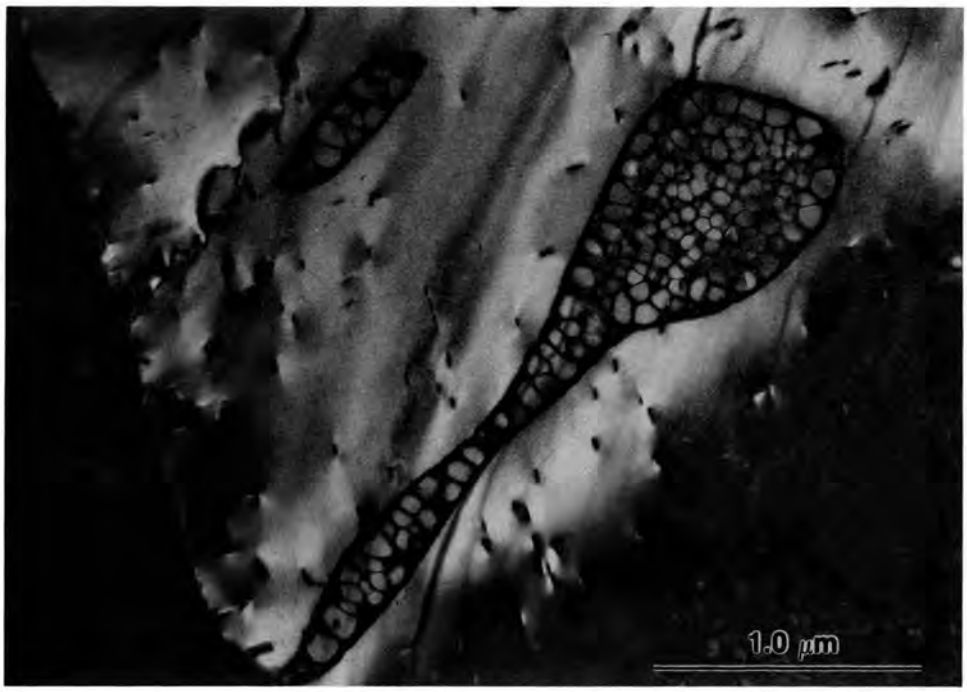

Fig. 5. Dark-field transmission electron micrograph of IC-47 (Ni—20 Al—15 Fe—0.2 B, at. %) showing scattered regions of cellular structure.

YE-12784

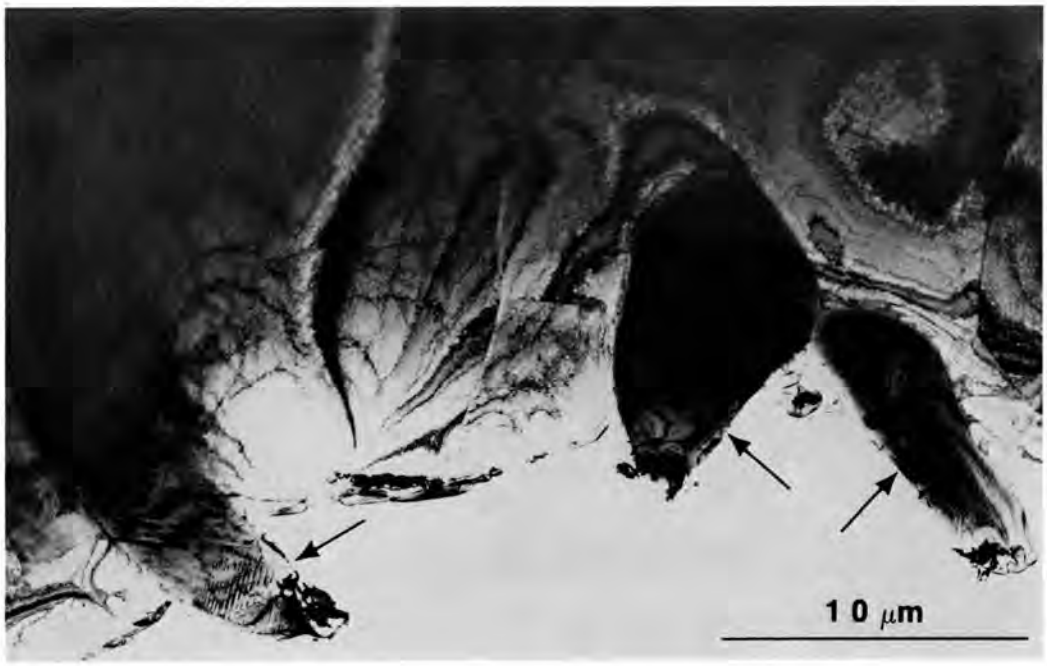

Fig. 6. Transmission electron micrograph of IC-47 (Ni—20 Al—15 Fe—0.2 B, at. %) showing martensitic beta prime particles.

7 at. %, depleted in iron by 1%, and depleted in nickel by 6% as compared with the matrix. This composition is approaching that of NiAl, in good agreement with the compositions found in the martensites formed by rapid solidification.[12]

In the aluminide with 20 at. % Fe (IC-65, 65 Ni—15 Al—20 Fe—0.2 B) the cellular structure has grown and nearly encompasses the entire specimen. Figure 7, a bright-field dark-field pair of micrographs, shows the dislocation cell structure in (*a*) and the cellular structure in (*b*). Note that the large clear ordered regions in (*b*) exactly correspond to the dislocation cells in (*a*). The dislocation cell walls surrounding the large clear ordered regions themselves consist of an ordered structure on a very fine scale. We compared EDS spectra between the large clear ordered regions and regions of the smaller cells. The electron beam was deliberately spread so as to produce an average composition that included several smaller cells and the separating disordered webs. These small

YE-12789

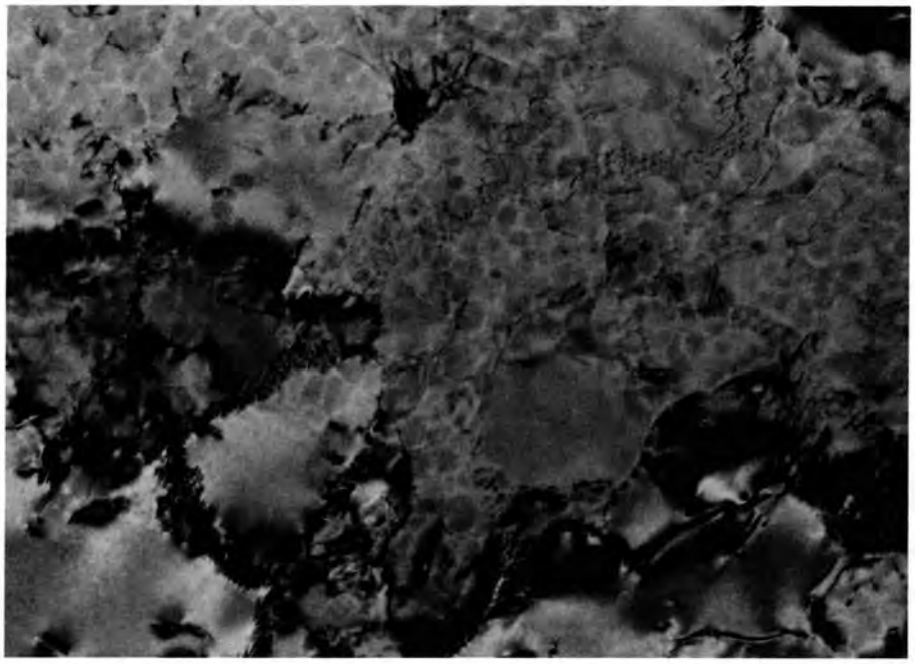

(*a*)

YE-12783

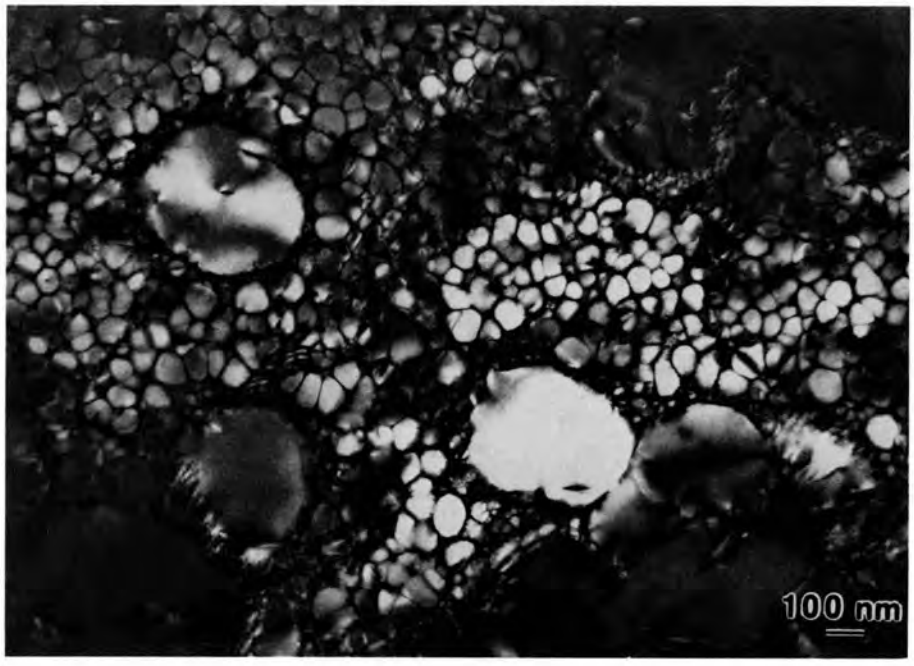

(*b*)

Fig. 7. Transmission electron micrographs of IC-65 (Ni—15 Al—20 Fe—0.2 B, at. %). (*a*) Bright field, showing the dislocation cell structure. (*b*) Dark field, showing the cellular structure.

cell regions were enriched in iron (9 at. %) and depleted in aluminum (5 at. %) and nickel (4 at. %) as compared with the matrix.

The alloy behavior of iron in Ni_3Al has been studied by Guard and Westbrook[13] and Ochiai et al.[14] Guard and Westbrook observed that the solubility of iron depends strongly on the relative concentrations of nickel and aluminum. The aluminide can dissolve a maximum of about 16 at. % Fe when aluminum and nickel are replaced by an equal amount of iron. Our study indicates that the maximum iron solubility should be slightly less than 15%. These results lead us to believe that iron atoms occupy both the nickel and aluminum sublattice sites (Fig. 8) available in the fcc ordered crystal structure. The sublattice occupation behavior of iron can be rationalized from the consideration of both chemical and structural effects of iron in Ni_3Al. Chemically, iron atoms are similar to nickel atoms. Structurally, iron behaves like aluminum, because it

CYN-514

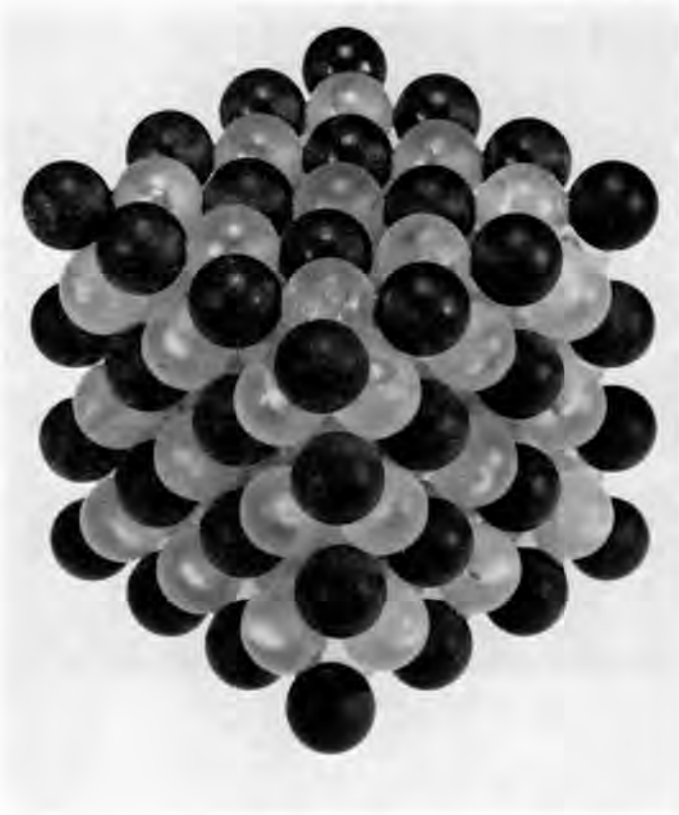

Fig. 8. Atomic model of Ni_3Al having a $L1_2$ ordered lattice structure. • Al sublattice sites. o Ni sublattice sites.

forms the $L1_2$ ordered crystal structure with nickel (i.e., Ni_3Fe). A balance of these two effects is that iron atoms occupy both the nickel and aluminum sublattice sites in Ni_3Al.

Beyond the solubility limit, second phases precipitate in Ni_3Al alloyed with sufficient amounts of iron. The iron additions of 15 and 20 at. % have produced a rather unique cellular structure — webs of disordered material surrounding ordered regions. Particles with a martensitic appearance have been observed in IC-47 but not in IC-39 and -65. The absence of the martensitic phase (transformed $B2$ phase) in IC-39 and -65 indicates that its stability is very sensitive to the aluminum-to-nickel ratio, in agreement with the ternary phase diagram of Ni-Al-Fe constructed by Rivlin and Raynor.[15]

No second phases were observed in Ni_3Al alloyed with up to 2 at. % Hf, Zr, Ti, or Mn. This is indicated in Fig. 9, showing the optical micrographs of the aluminides containing 0.5, 1.0, and 1.5 at. % Hf. All exhibited essentially a single-phase grain structure with no indication of formation of second phases. The TEM in Fig. 10 also revealed no precipitation of second-phase particles within or along grain boundaries.

The nickel-iron aluminides in Table 3 also have essentially a single-phase grain structure [Fig. 11(a)], except those containing 0.16 to 0.8 at. % C (0.04 to 0.2 wt % C) [Fig. 11(b) and (c)]. The morphology of precipitates in IC-32 was studied in detail by TEM. The particles in Fig. 11(c) were identified as titanium carbide (TiC) with a lattice parameter of 0.43 nm. Analysis by EDS also showed that the metal content of these particles was nearly pure titanium. The particles ranged in diameter from 0.1 to 1.0 μm and covered about 2% of the areas examined (Fig. 12). A preliminary analysis of the orientation relationship of these particles to the matrix showed that the $(001)_{ppt}$ is parallel to the $(001)_{matrix}$ and the $[200]_{ppt}$ is parallel to the $[220]_{matrix}$. This is not the cube-on-cube relationship that is more commonly observed for TiC precipitation.

Y-196523

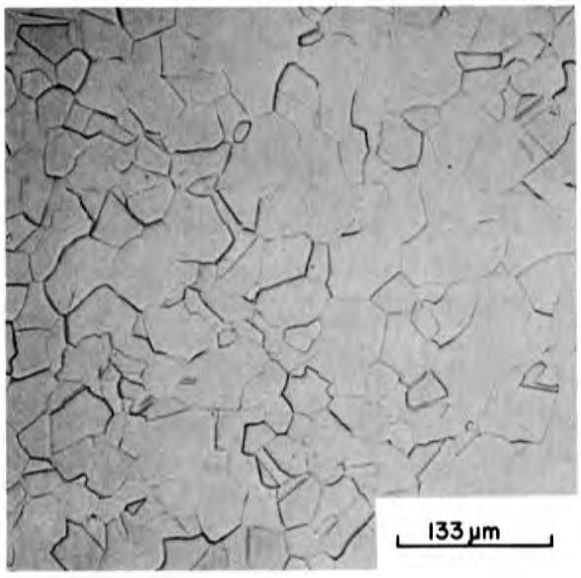

(*a*)

Y-195325

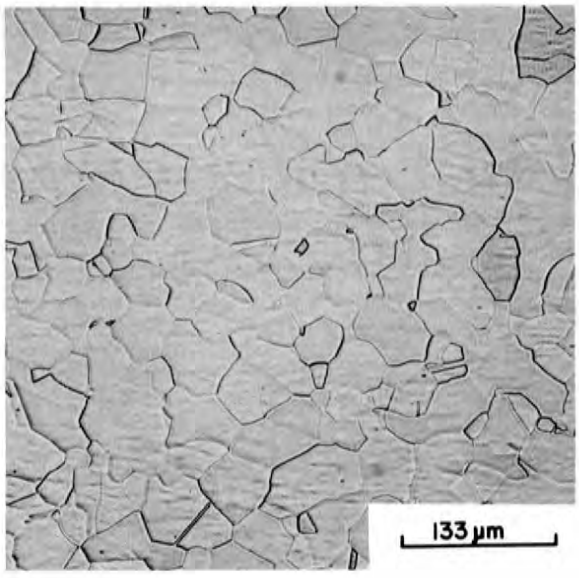

(*b*)

Y-195328

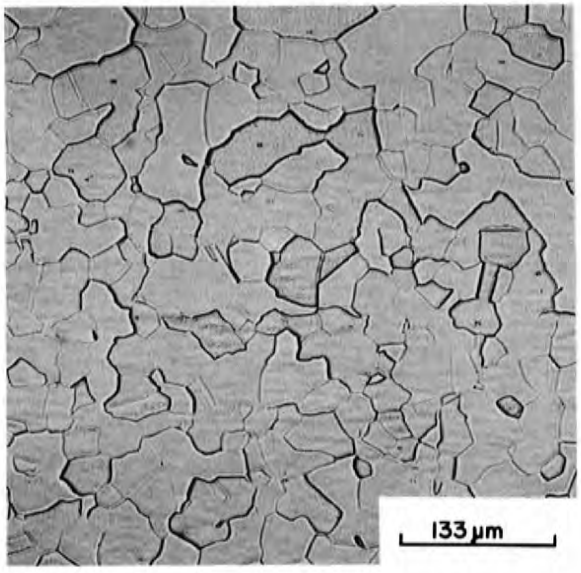

(*c*)

Fig. 9. Optical micrographs of the aluminides containing (*a*) 0.5, (*b*) 1.0, and (*c*) 1.5 at. % Hf.

YE-12592

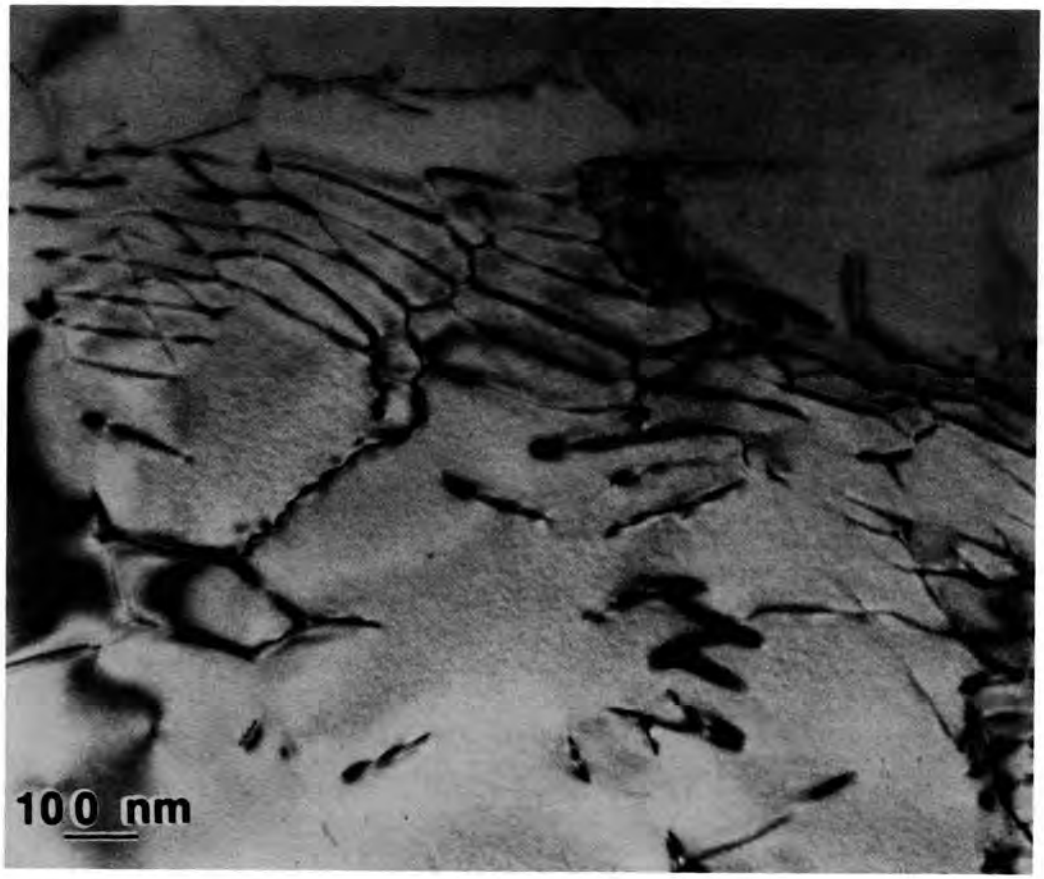

Fig. 10. Transmission electron micrograph of the aluminide containing 0.5 at. % Hf, showing no precipitation of second phases within grains or along grain boundaries.

TENSILE PROPERTIES

Tensile properties of aluminides were determined at temperatures to 1000°C in vacuum. Tensile tests were performed on sheet specimens (with a gage section of 12.7 mm × 0.8 mm) at a crosshead speed of 42 μm/s. The test temperature was monitored by a Pt vs Pt—10% Rh thermocouple located at the center of the gage section.

The tensile properties of Ni_3Al alloyed with iron are reported in Table 4 and shown in Fig. 13 as functions of iron concentration. The yield stress increased significantly with increasing iron concentration at room temperature, 600°C, and 850°C, but not at 1000°C. The tensile

Y-189079

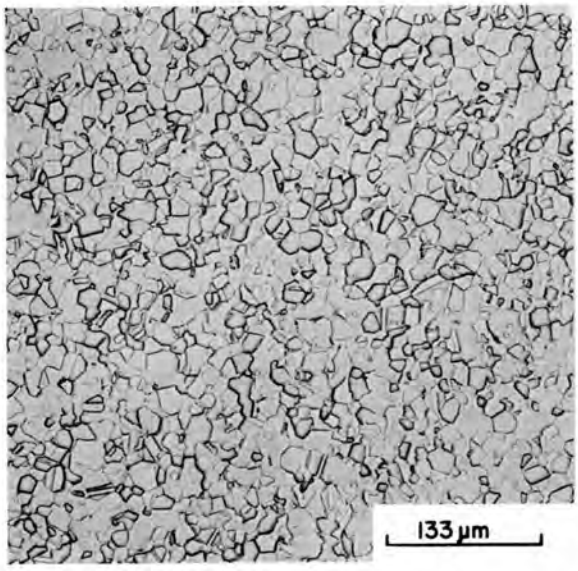

(a)

Y-195326

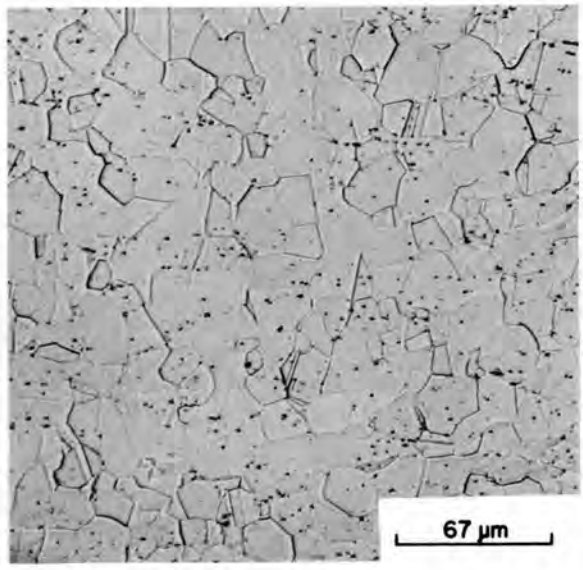

(b)

Y-189439

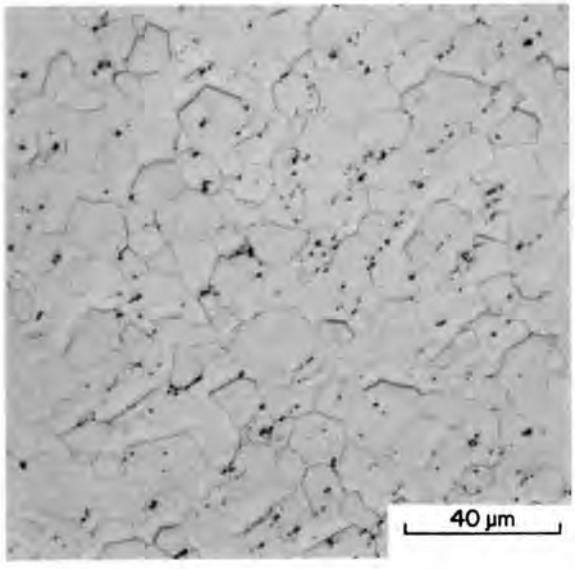

(c)

Fig. 11. Optical micrographs of nickel-iron aluminides. (*a*) Single-phase grain structure in IC-25 (Ni–10 Fe–19 Al–0.5 Mn–0.5 Ti–0.2 B, at. %). (*b*) Precipitation of carbide particles in IC-63 (Ni–10 Fe–20 Al–0.5 Mn–0.5 Hf–0.2 B–0.16 C). (*c*) Precipitation of carbide particles in IC-32 (Ni–10 Fe–19.0 Al–0.5 Mn–0.9 Ti–0.2 B–0.4 C).

YE-12592

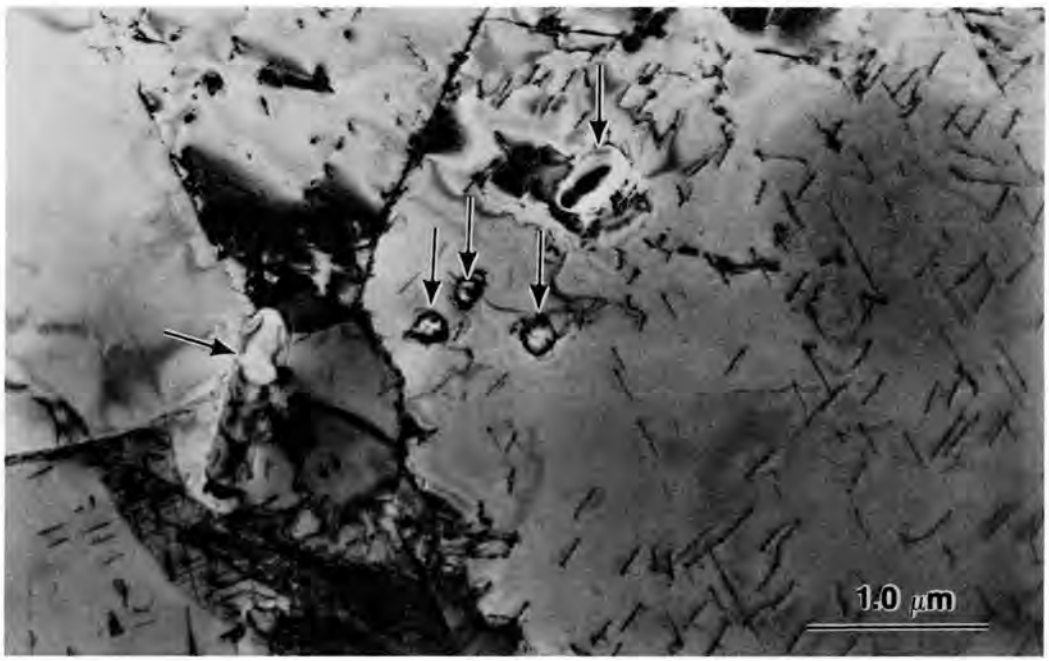

Fig. 12. Transmission electron microstructure of IC-32 specimen annealed for 30 min at 1000°C, showing the morphology of TiC particles (arrows).

elongation decreased with increasing iron concentration at room temperature and 600°C but became less dependent at 850 and 1000°C. The ductility of the aluminides also decreased with increasing test temperature and reached a minimum of about 5% at 850°C. The ultimate tensile strength was generally not sensitive to iron concentration and showed only a moderate decrease at elevated temperatures.

Figure 14 shows the effect of hafnium additions on tensile properties of boron-doped Ni_3Al at room temperature, 600, 850, and 1000°C. The yield stress increased substantially with the hafnium concentration at all four temperatures. Surprisingly, the slope of the curve in Fig. 14 increases with temperature and is steepest at 850°C; that is, the hafnium is more effective in strengthening Ni_3Al at 850°C than at the other temperatures.

The ductility of Ni_3Al is not sensitive to the hafnium concentration to about 1 at. % at room temperature and to about 1.5 at. % at 600 and

Table 4. Tensile properties of nickel-iron aluminides annealed for 1 h at 1050°C

Alloy	Iron concentration (at. %)	Yield strength		Ultimate tensile strength		Elongation (%)
		(MPa)	(ksi)	(MPa)	(ksi)	
		Room temperature				
IC-15	0	238	34.7	1304	189.3	53.0
IC-64	6	311	45.1	1229	178.4	43.3
IC-46	10	369	53.6	1264	183.4	49.6
IC-47[a]	15	540	78.4	1364	197.9	42.1
IC-39[b]	15	527	76.5	1343	195.0	36.0
IC-65	20	637	92.5	1277	185.4	29.4
		600°C				
IC-15	0	497	72.2	1106	160.5	43.3
IC-64	6	604	87.6	902	130.9	29.5
IC-46	10	649	94.2	873	126.7	20.1
IC-47[a]	10	648	94.1	930	135.0	14.5
IC-39[b]	15	648	94.1	930	135.0	14.5
IC-65	20	657	95.3	1040	150.9	17.9
		850°C				
IC-15[c]	0	474	68.8	648	94.1	11.3
IC-64	6	494	71.7	599	87.0	4.7
IC-46	10	531	77.0	603	87.5	5.9
IC-47[a]	15	469	68.1	489	70.9	11.4
IC-39[b]	15	561	81.4	584	84.8	4.9
		1000°C				
IC-15[c]	0	284	41.2	364	52.9	14.1
IC-64	6	253	36.7	359	52.2	8.0
IC-46	10	294	42.7	323	46.9	12.1
IC-47[a]	15	213	30.9	225	32.7	25.2
IC-39[b]	15	277	40.2	301	43.7	11.8

[a]Ni–20 Al–15 Fe–0.2 B (at. %).

[b]Ni–17.5 Al–15 Fe–0.2 B (at. %).

[c]Specimens were annealed for 30 min at 1000°C.

850°C (Fig. 14). Above these levels, the ductility of the hafnium-modified aluminides decreases significantly. At 1000°C, the ductility decreases continuously with increase in hafnium, and the aluminide loses its ductility at 1.0% Hf. Further work is needed to improve the ductility of hafnium-modified aluminides at higher temperatures.

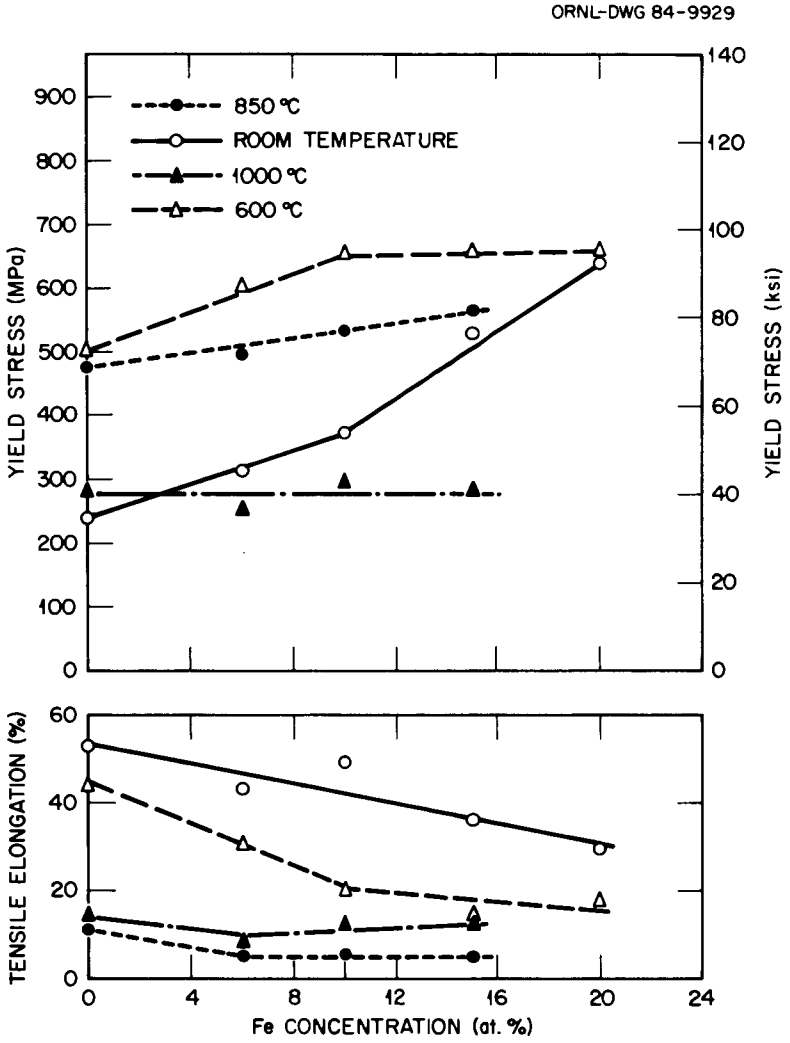

Fig. 13. Yield stress and tensile elongation as functions of iron concentration in Ni_3Al.

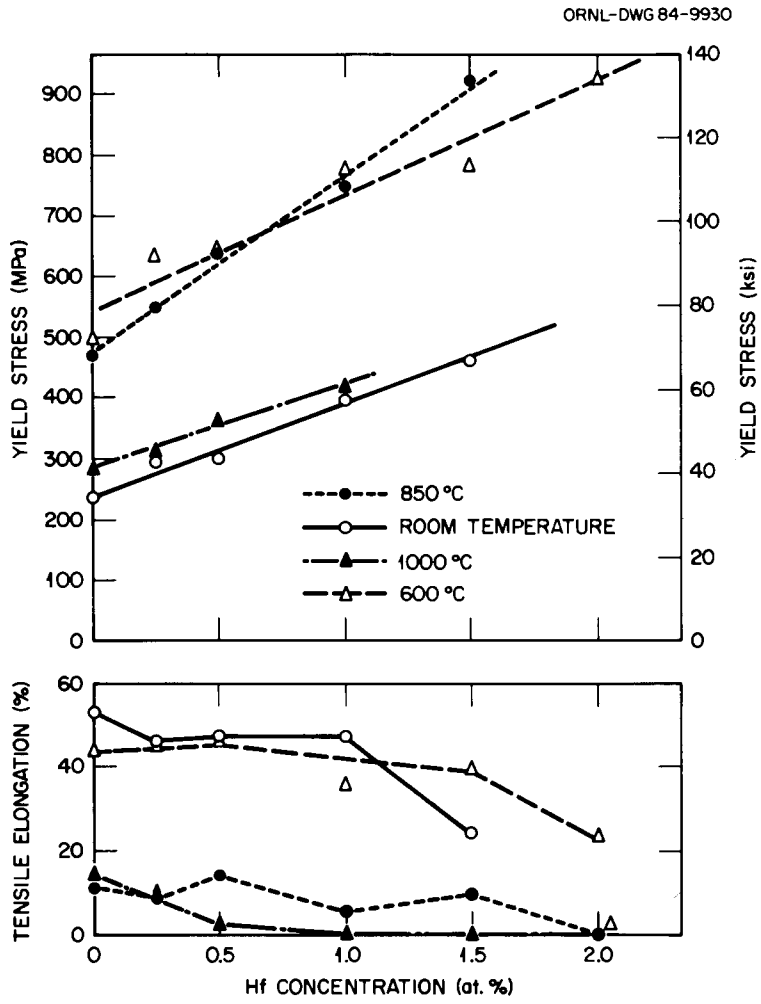

Fig. 14. Yield stress and tensile elongation as functions of hafnium concentrations in Ni_3Al.

Figure 15 shows yield stress as a function of temperature for boron-doped Ni_3Al (IC-15) and boron-doped Ni_3Al modified with 0.5% Hf (IC-50) and 0.5% Ti (IC-74). Unlike that of conventional alloys, the yield strength of IC-15 increases with increasing temperature and reaches a maximum around 650°C. The positive temperature dependence of the yield strength, which has been observed in other $L1_2$ ordered alloys,[1,2] is generally attributed to a thermally activated hardening process[16] in connection with the (111) slip systems. The strength starts to decrease with temperature above 650°C, corresponding to a gradual change in slip systems from (111) to (100) planes.[17,18]

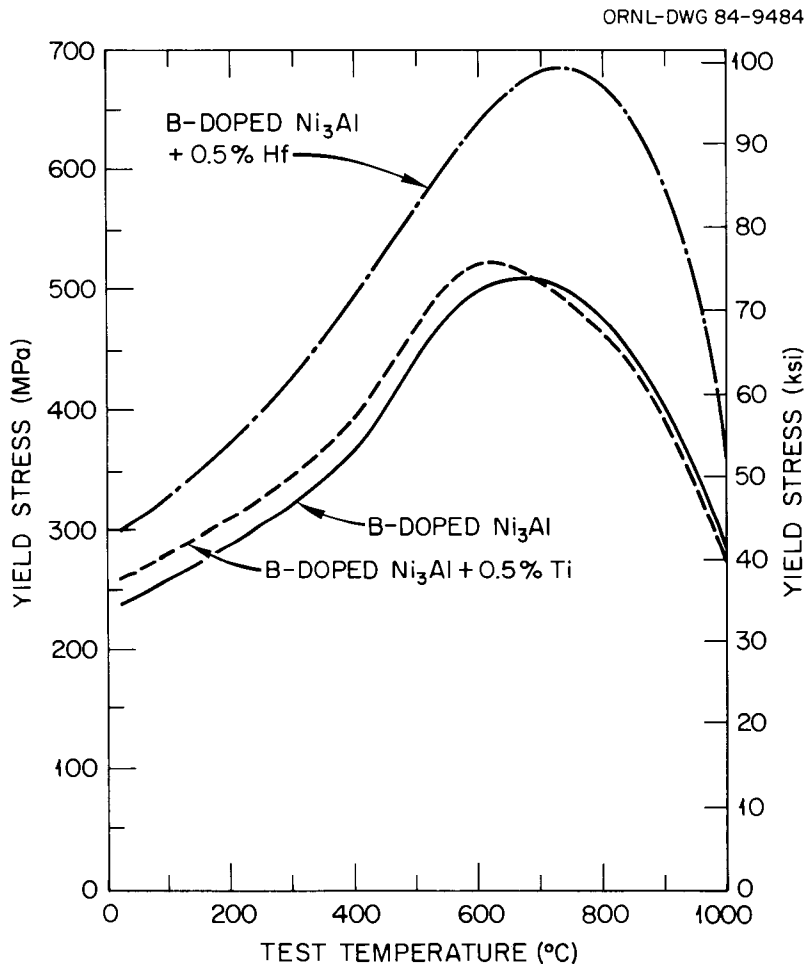

Fig. 15. Yield stress as a function of test temperature for boron-doped Ni_3Al, boron-doped Ni_3Al + 0.5% Ti, and boron-doped Ni_3Al + 0.5% Hf.

Hafnium and titanium are chemically similar to each other; however, their hardening effects on Ni_3Al are distinctively different. Alloying with 0.5% Ti causes only a small increase in the strength of Ni_3Al at temperatures below 700°C. Hafnium, on the other hand, substantially hardens Ni_3Al at all test temperatures. The unique hardening effect of hafnium, which is not well understood, may be related to a lowering of the antiphase boundary energy on (100) planes relative to (111) planes, thereby further promoting cross slip of superlattice dislocations onto (100) planes.

Figures 16 and 17 compare the yield stress and ultimate tensile strength of the advanced aluminides we developed with the same properties

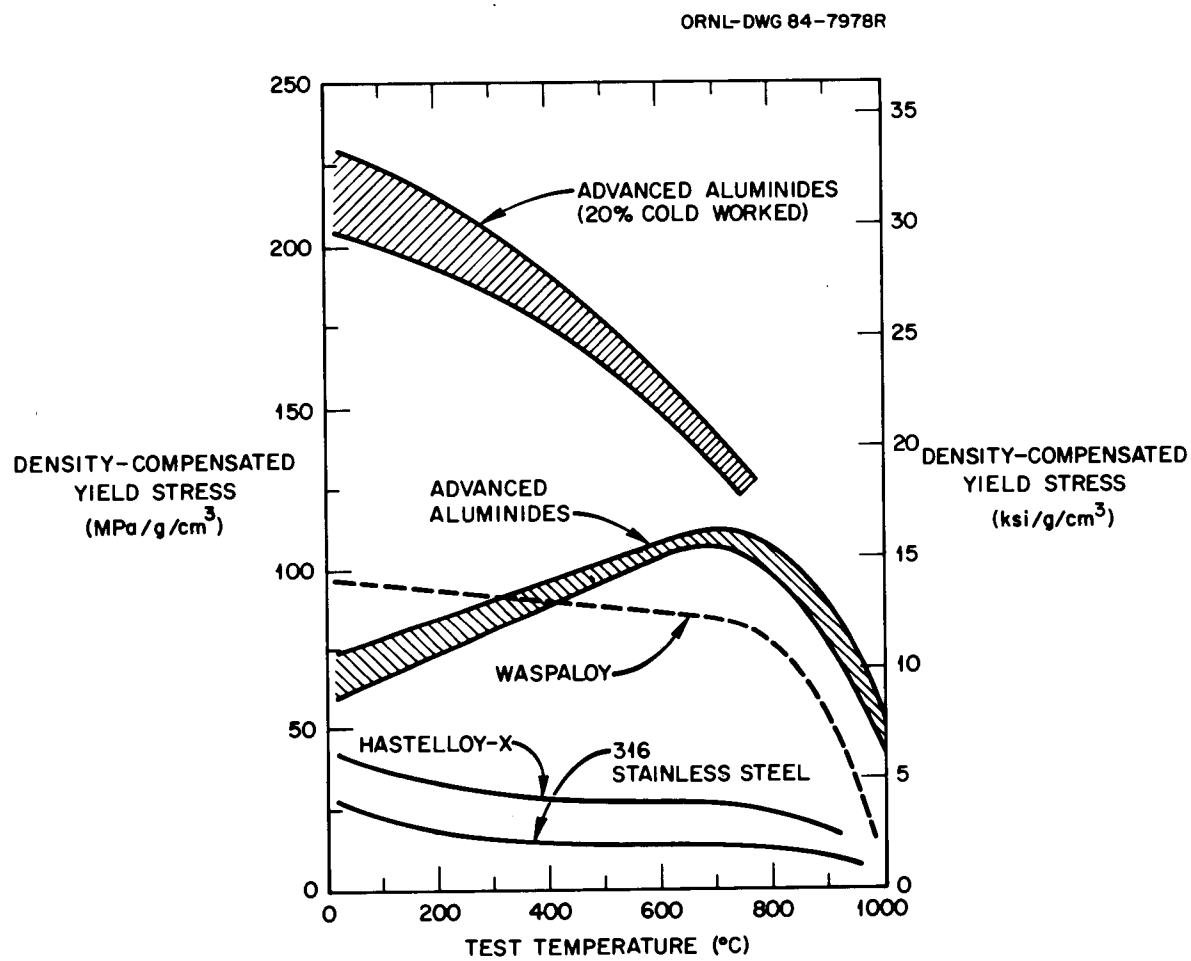

Fig. 16. Comparison of density-compensated yield stress (as a function of temperature) of our advanced aluminides with commercial alloys.

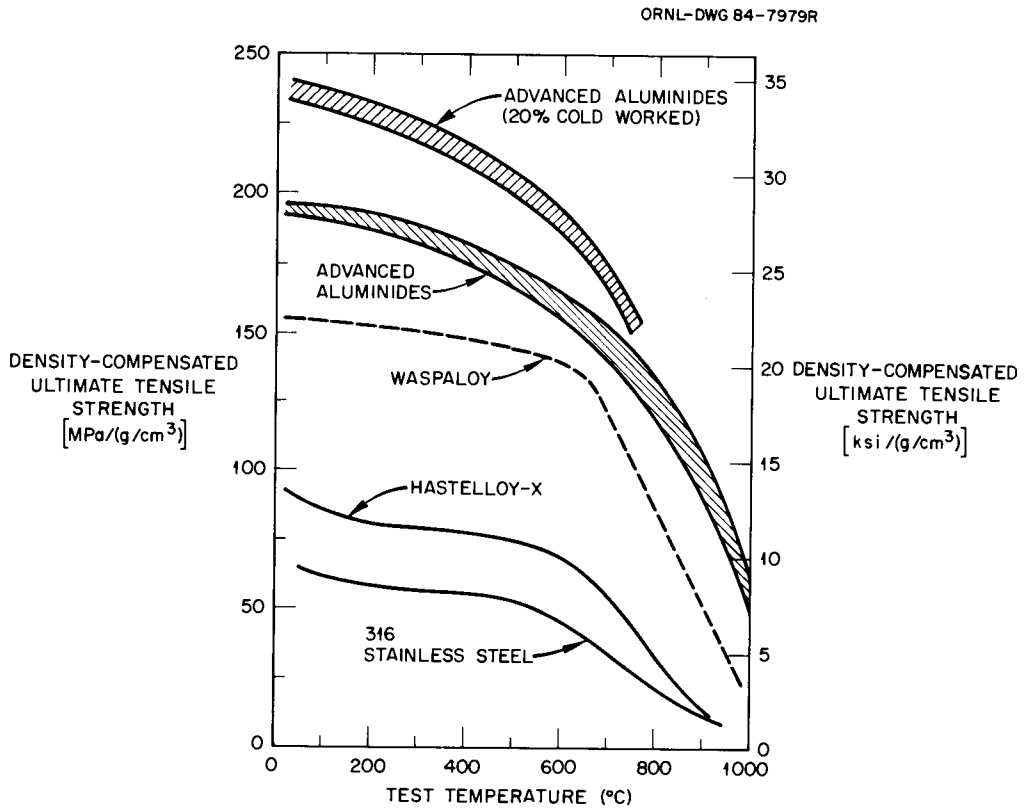

Fig. 17. Comparison of density-compensated ultimate tensile strength (as a function of temperature) of advanced aluminides with commercial alloys.

of wrought commercial alloys. The aluminides are less dense than the commercial alloys by about 10%; hence the comparison is made on a density-compensated basis. The specific yield strength of the aluminides is substantially higher than that of type 316 stainless steel and Hastelloy X at all temperatures and is also higher than that of Waspaloy (one of the stronger wrought nickel-base superalloys in use) above 400°C. The yield strength of the aluminides can be further increased by cold work as shown in Fig. 16. The cold-work effect appears to diminish above 800°C. In terms of ultimate tensile strength, the aluminides in both well-annealed and cold-worked conditions are stronger than the commercial alloys at all temperatures (Fig. 17).

AIR OXIDATION

Coupons of selected aluminides recrystallized for 1 h at 1050°C were exposed to air for study of oxidation. The samples were periodically (1–3 d) removed from the furnaces for weight measurements. Figure 18 shows the oxidation curves for four aluminides oxidized for 500 to 600 h at 1000°C. The base aluminide, IC-15, and the two hafnium-modified aluminides, IC-50 and IC-68, all exhibited consistent weight gain during the cyclic oxidation. Among them, IC-15 showed the lowest weight gain and IC-68, containing 9.5 at. % Fe and 0.5 at. % Hf, the highest, with IC-50 close to IC-15. The aluminide IC-46, containing 10 at. % Fe, started to show weight loss after about 100-h exposure.

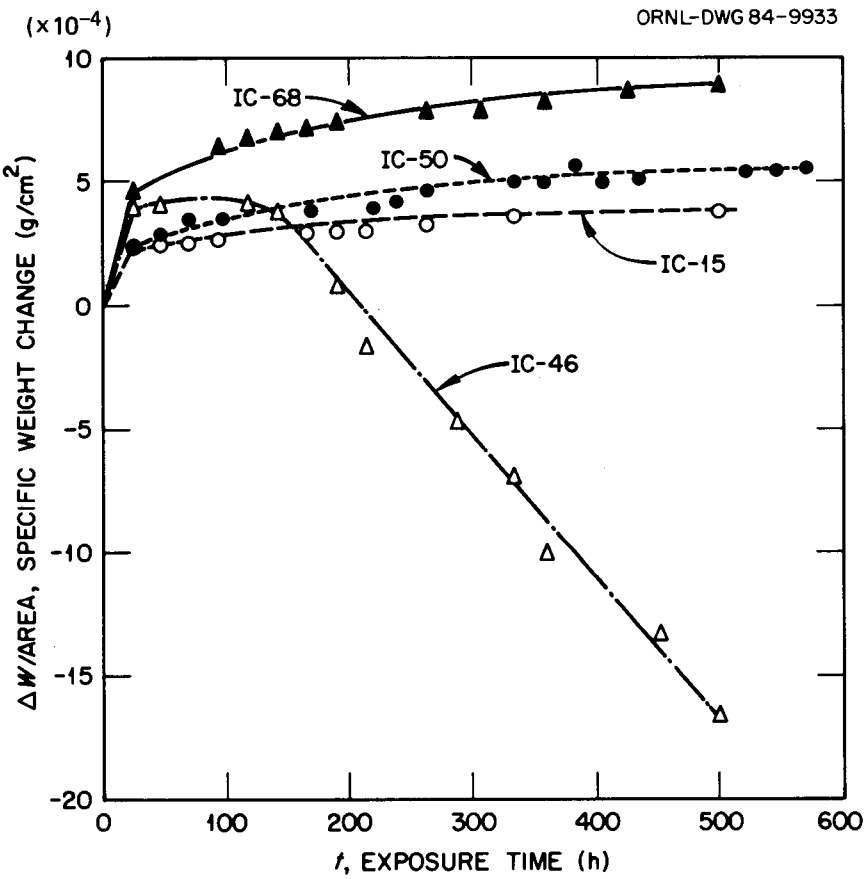

Fig. 18. Weight gain as a function of exposure time for nickel-iron aluminides oxidized in air at 1000°C. The aluminide IC-15 (Ni–24% Al–0.2% B, at. %) showed the lowest weight gain and IC-68 (Ni–9.1% Fe–20% Al–0.5% Mn–0.5% Hf–0.5% Ta–0.16% C–0.2% B) the highest, with IC-50 (Ni–23.5% Al–0.5% Hf–0.2% B) close to IC-15. The aluminide IC-46 (Ni–20 Al–10 Fe–0.2 B) started to show weight loss after about 100-h exposure.

The IC-15 sample showed very slight spalling, and flaked oxide scales were visible only under a microscope. No spalling was detected in IC-50 and IC-68, indicating that a small amount of hafnium improves the adhesion of oxide scales. The severe flaking of IC-46 oxide scale is presumably due to a combination of low aluminum level and the lack of hafnium additions.

Figure 19 is a plot of specific weight gain versus $t^{1/2}$, where t is exposure time at 1000°C. A linear relation holds quite well for IC-15, -50, and -68, indicating parabolic oxidation behavior for these aluminides after an initial higher rate. The parabolic oxidation law obviously does not apply in the case of IC-46 because of the severe spalling of the oxide scale during the cyclic oxidation.

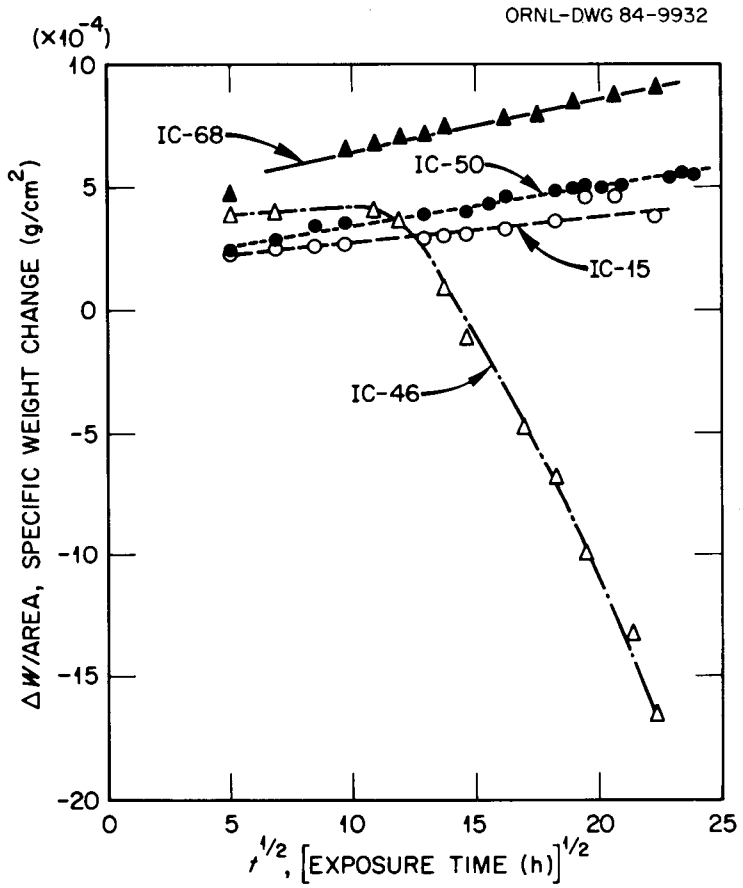

Fig. 19. Weight gain versus $t^{1/2}$ (t = exposure time, h) for nickel-iron aluminides oxidized in air at 1000°C.

Figures 20 and 21 compare the weight gain of hafnium-modified nickel aluminides (IC-50 and -72) with that of commercial alloys oxidized at 1000 and 1100°C, respectively. The weight change of IC-50 after about 150 h at 1000°C is lower that those of Hastelloy X and type 316 stainless steel by factors of 2 and 200, respectively. A rise of oxidation temperature from 1000 to 1100°C increased the oxidation rate of the aluminide IC-72 by a factor of about three. However, the 1100°C oxidation resulted in a severe spalling, bulging, and wrinkling of Hastelloy X samples (Fig. 22), probably because of the combined effects of extensive oxidation and oxidation-induced internal stresses.

The superior oxidation resistance of the aluminides comes from the formation of compact adherent films of oxides in oxidizing environments. Both x-ray diffraction and electron microprobe analyses revealed Al_2O_3 films on the oxidized aluminide samples.

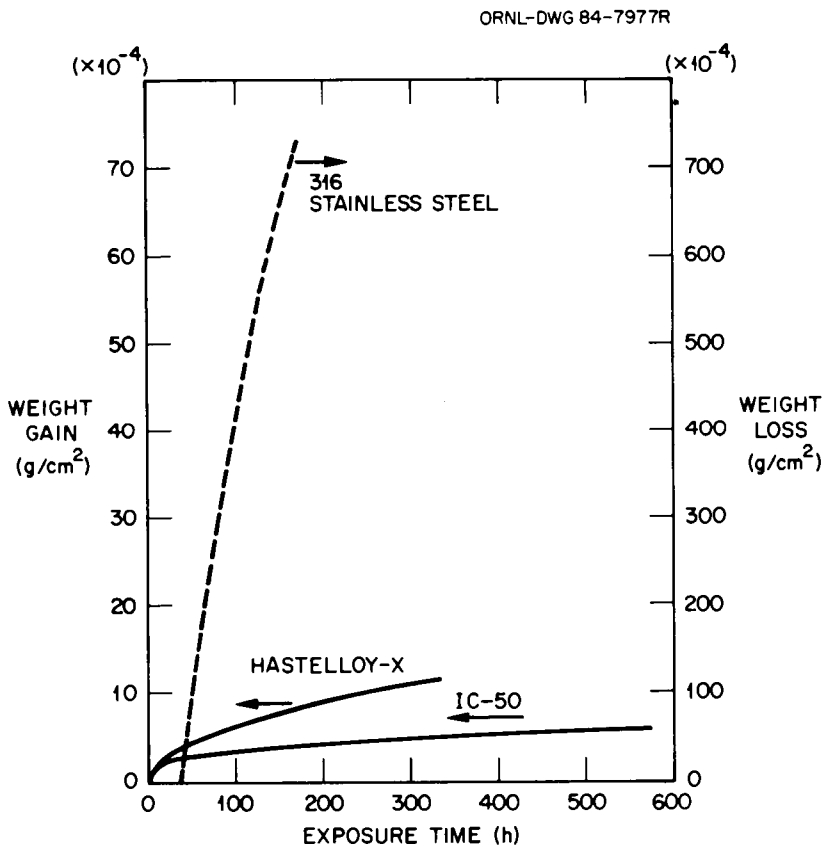

Fig. 20. Comparison of 1000°C air oxidation of the aluminide IC-50 with Hastelloy X and type 316 stainless steel.

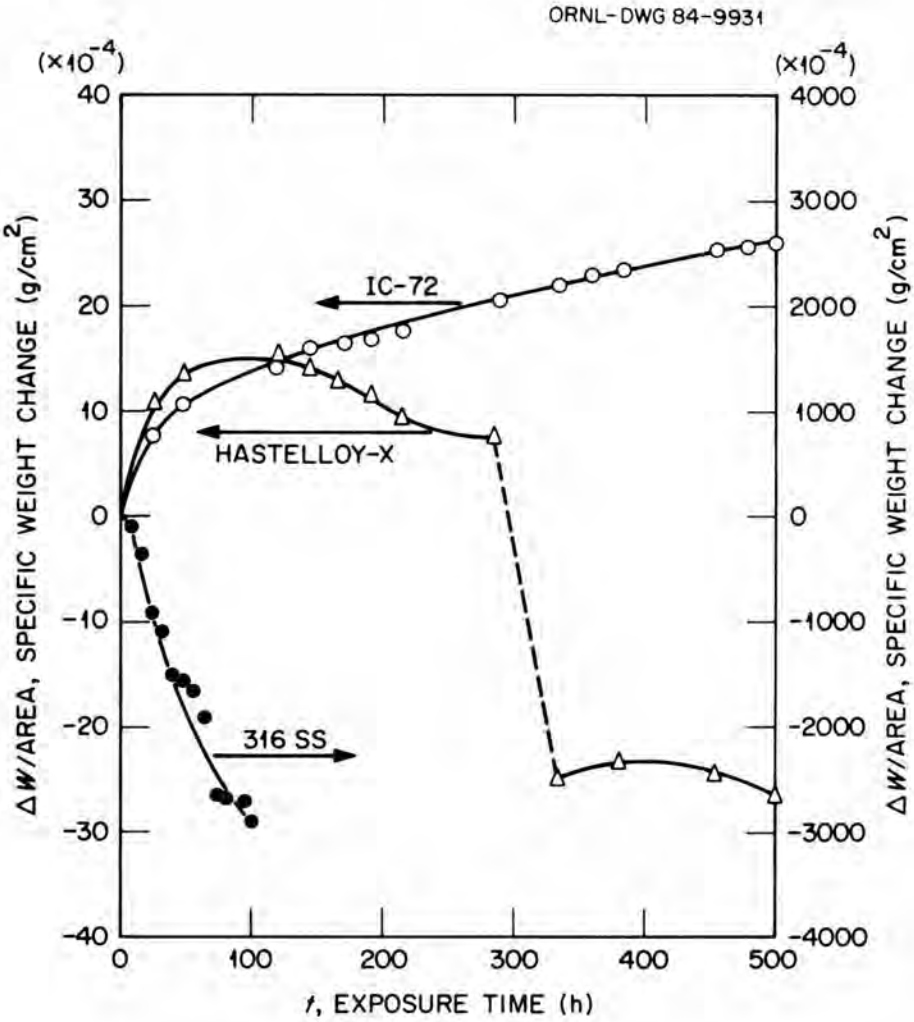

Fig. 21. Comparison of 1100°C air oxidation of the aluminide IC-72 with Hastelloy X and type 316 stainless steel.

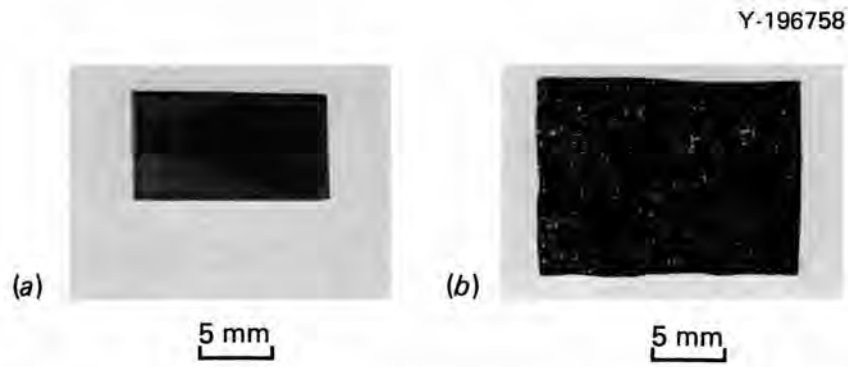

Fig. 22. Appearance of (*a*) nickel aluminide (IC-72) and (*b*) Hastelloy X specimens subjected to cyclic oxidation in air for 500 h at 1100°C.

CORROSION OF ALUMINIDES IN SULFIDIZING ENVIRONMENTS

The internal components in an atmospheric fluidized-bed combuster (AFBC) become coated with a compact deposit of $CaSO_4$, CaO, and ash during the combustion of coal with limestone. The sulfate deposit on the hot metal surfaces has been suggested as the cause of the observed accelerated oxidation-sulfidation corrosion,[19] and recent work supports this suggestion.[20]

This study characterizes the corrosion of nickel-iron aluminides by $CaSO_4$ and/or SO_2 and O_2, its decomposition products, to the extent that the mechanism of the accelerated oxidation-sulfidation corrosion can be understood and the effect of alloy composition is known. Thus, the goal of this study is to provide input into the development of sulfidation-resistant alloys suitable for coal utilization systems.

APPARATUSES AND EXPERIMENTAL PROCEDURES

Two types of apparatuses have been used (Fig. 23). The first consists of an evacuated quartz tube containing a supply of $CaSO_4$ and a test specimen either embedded in the $CaSO_4$ or suspended in the vapor phase above it. This test suffers from the fact that the final oxygen and sulfur pressures in the tube depend on the extent of oxygen depletion in the gas-phase decomposition products of $CaSO_4$ (see below). Extensive oxidation of a sample can lead to large increases in the sulfur partial pressure, producing very severe test conditions. The advantages of the test lie in its simplicity and in the fact that the absence of extensive attack is a good indication that the test sample forms an oxide that is relatively impervious to sulfur penetration.

The other apparatus is a closed circulating loop in which a carrier gas (helium) passes over a heated bed of $CaSO_4$ and establishes a steady-state gas-phase concentration of the $CaSO_4$ decomposition products, which then react with specimens suspended in the loop. The p_{S_2}/p_{O_2} ratio can be varied through additions of O_2 or SO_2 to the carrier gas. Test temperatures range from 650 to 871°C.

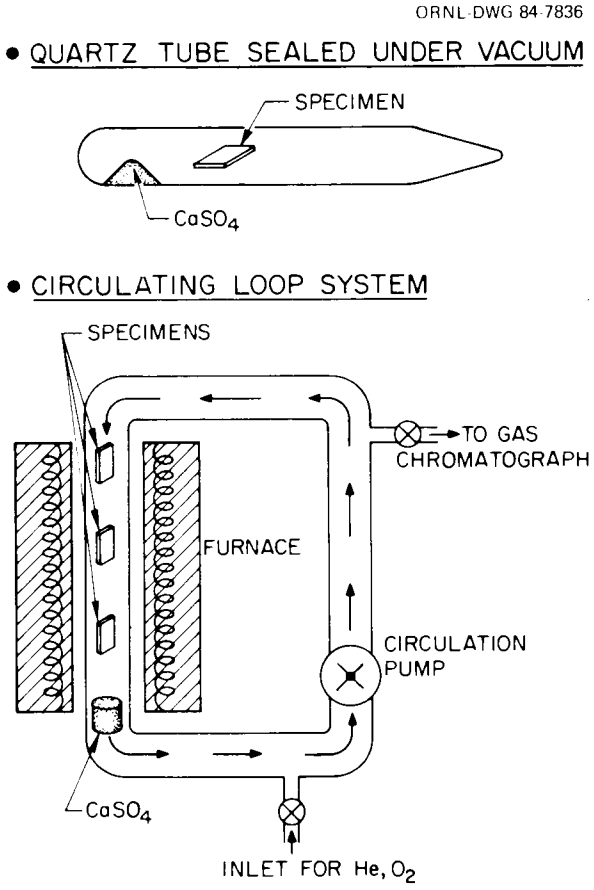

Fig. 23. Apparatuses for sulfidation testing.

Alloy strips with the compositions listed in Table 5 and dimensions of about 0.6 by 3 by 12 to 25 mm were mechanically polished, rinsed in a solvent, then corrosion tested for 168 h (1 week). One group was preoxidized in air, and a second group was preoxidized in wet hydrogen before corrosion testing. The corrosion behavior was observed by weight changes, bend tests, scanning electron microscopy, metallography, and microprobe analyses.

CORROSION IN QUARTZ CAPSULE TESTS

Table 6 compares the weight change and bend ductility of iron and nickel aluminides with two commercial alloys exposed to $CaSO_4$ powder in a capsule at 871°C. Both IC-50 and IC-63 were completely embrittled by the test. In contrast, Hastelloy X and type 304 stainless steel were not

Table 5. Alloys screened for corrosion resistance to $CaSO_4$

Alloy	Nominal composition	
	(wt %)	(at. %)
IC-50	Ni–12.3 Al–1.7 Hf–0.05 B	Ni–23.5 Al–0.5 Hf–0.24 B
IC-63	Ni–10.6 Fe–10.2 Al–1.7 Hf–0.5 Mn–0.05 B	Ni–10 Fe–20 Al–0.5 Hf–0.5 Mn–0.24 B
IC-10	Ni–30.6 Al	Ni–49 Al
IC-15	Ni–12.7 Al–0.05 B	Ni–24 Al–0.24 B
IC-40	Ni–10.4 Al–10.8 Fe–5 Cr–0.05 B	Ni–19.9 Al–10 Fe–5 Cr–0.26 B
IC-83	Ni–12 Al–2 Cr–1.7 Hf–0.05 B	Ni–23 Al–2 Cr–0.5 Hf–0.26 B
LRO-79	Ni–15.2 Fe–10.9 V–4.9 Al–3.8 Cr–3.2 Hf–0.5 Mn–0.01 B–0.004 Ce	Ni–15 Fe–11.8 V–10 Al–4 Cr–1 Hf–0.02 Ce–0.5 Mn
Hastelloy X	Ni–22 Cr–9 Mo	Ni–25–5.5 Mo
Type 304 SS	Fe–18 Cr–10 Ni	Fe–19.2 Cr–9.4 Ni
FA-2	Fe–13.3 Al	Fe–24 Al
Iron	100 Fe	100 Fe

Table 6. Corrosion of alloys by $CaSO_4$ in an evacuated capsule at 871°C

Alloy	Pre-oxidation temperature (°C)[a]	Weight change (%)		Bend ductility at room temperature	
		Control	Control + $CaSO_4$	Control	Control + $CaSO_4$
Hastelloy X	800	0.010	0.010	Ductile	Ductile
Type 304 SS	800	0.150	–0.005	Ductile	Ductile
FA-2	800	0.078	0.121	Brittle	Brittle
IC-50	1000	0.267	0.857	Ductile	Brittle
IC-63	1000	0.508	19.753	Ductile	Brittle

[a]96 h in air.

embrittled. Because the iron aluminide, FA-2, was not ductile initially, its resistance to $CaSO_4$ embrittlement was assumed to be good from the very small weight change.

Table 7 lists the data for capsule tests of IC-50 at three temperatures, two surface treatments, and location of the specimen relative to the $CaSO_4$. Two significant results were noted. First, the specimens pretreated in wet H_2 were resistant to $CaSO_4$ embrittlement at 650°C and were marginally resistant but still superior to the vacuum-annealed specimens at 750 and 871°C. Both pretreatments are expected to result in

Table 7. Corrosion of Ni—23.5 at. % Al—0.5 at. % Hf—0.2 at. % B by $CaSO_4$

(IC-50, 168-h exposure to corrosion environment)

Specimen pretreatment[a]	Specimen location	Test results	
		Weight change ΔW (%)	Bend test
	871°C		
Vacuum annealed	In $CaSO_4$	3.4	Brittle
Wet H_2 annealed	In $CaSO_4$	1.4	Brittle and ductile[b]
Vacuum annealed	In $SO_2 + O_2$[c]	1.1	Brittle
Wet H_2 annealed	In $SO_2 + O_2$[c]	3.6	Brittle
	750°C		
Vacuum annealed	In $CaSO_4$	−0.9	Brittle
Wet H_2 annealed	In $CaSO_4$	−0.02	Ductile
Vacuum annealed	In $SO_2 + O_2$[c]	−2.6	Brittle
Wet H_2 annealed	In $SO_2 + O_2$[c]	3.4	Brittle
	650°C		
Vacuum annealed	In $CaSO_4$	2.1	Brittle
Wet H_2 annealed	In $CaSO_4$	0.2	Ductile
Vacuum annealed	In $SO_2 + O_2$[c]	2.1	Brittle
Wet H_2 annealed	In $SO_2 + O_2$[c]	0.2	Ductile

[a]Vacuum anneal 1 h at 1000°C; $\Delta W = \pm 0.02\%$. Hydrogen anneal 24 h at 1000°C in 87 kPa He, 11 kPa H_2, and 3 H_2O (0.86, 0.11, and 0.03 atm).

[b]Ends brittle; center ductile.

[c]Specimens outside platinum foil envelopes contain $CaSO_4$ powder.

Al_2O_3 film formation because the residual gases in a vacuum consist of H_2O, CO, and H_2 and are, therefore, reducing to nickel. The difference in their corrosion behavior is, therefore, assumed to arise from a difference in film thickness because the weight change was about 0.02% for the vacuum-annealed specimens and 0.06 to 0.9% for the wet H_2 anneal (footnote *a*, Table 7). Second, embrittlement of the alloy clearly did not depend on its physical contact with $CaSO_4$ because similar results were obtained for specimens buried in $CaSO_4$ and for specimens exposed to only O_2 and SO_2, the decomposition products of $CaSO_4$. Therefore, the corrosion may occur not only as a result of reactions at a $CaSO_4$-metal interface as suggested previously[19,20] but also as a consequence of a reaction of an alloy with the gaseous decomposition products of $CaSO_4$. In both mechanisms sulfidation depends on a concurrent oxidation process.

The decomposition of $CaSO_4$ may be written as

$$CaSO_4 \rightleftarrows CaO + SO_2 + 1/2\ O_2 \rightleftarrows 1/2\ S_2 + 3/2\ O_2\ CaO\ ,$$

and the equilibrium constant is

$$k_{CaSO_4} = (p_{O_2})^{3/2}(p_{S_2})^{1/2}\ . \qquad (1)$$

At 871°C the equilibrium p_{S_2} is about 10^{-19} Pa (10^{-24} atm), which is well below the decomposition pressure of FeS or Ni_3S_2.

Because the oxygen in the sealed quartz capsules can be depleted through the formation of a metal oxide, test conditions in the capsule can become very severe by the increase in sulfur pressure required to maintain the equality in Eq. (1). We suggest this mechanism to account for the very heavy attack suffered by the Ni_3Al-base alloys. The surface of an IC-50 specimen (Ni—23.5 at. % Al—0.5 at. % Hf—0.2 at. % B) exposed for 168 h at 871°C is shown in Fig. 24. X-ray spectra of the spherical particles on the surface show them to contain nickel and sulfur, and their shape suggests that at temperature they were molten and consisted of the Ni-Ni_3S_2, which melts at about 645°C. The formation of molten Ni_3S_2 would account for the severity of the corrosion and would indicate a minimum

ORNL-PHOTO 0265-84

Fig. 24. Surface of an Ni—23.5 Al—0.5 Hf—0.2 B, at. %, (IC-50) specimen exposed to the decomposition products of $CaSO_4$ for 168 h at 871°C in a sealed evacuated quartz capsule.

sulfur pressure in the quartz capsule of about 30 mPa (3×10^{-7} atm), the decomposition pressure of Ni_3S_2 at 871°C. The specimen shown in Fig. 24 was not in physical contact with the $CaSO_4$, but a similar sample buried in $CaSO_4$ powder also underwent severe attack. The scale contained the same Ni_3S_2 spherules, and calcium could be detected, raising the possibility of additional scale fluxing by CaO.

The lack of corrosion of the commercial alloys tested was surprising, especially in the case of Hastelloy X, where the atomic percent nickel is almost the same as in Ni_3Al. Figure 25 shows the surface of a Hastelloy X specimen exposed for 168 h at 871°C to $CaSO_4$ in a standard quartz capsule that also contained an Ni_3Al (Ni—23.5 at. % Al—0.5 at. % Hf—0.2 at. % B) specimen. The latter specimen was heavily attacked (see Fig. 24). The Hastelloy X, on the other hand, was only mildly attacked. Its surface was covered with a thin layer of Cr_2O_3, which spalled badly on cooling, revealing a second, underlying layer of corrosion products. X-ray spectra from this layer indicated the presence of S as well as Ni, Fe, and Cr.

M-17061

Fig. 25. Surface of a Hastelloy X specimen exposed to the decomposition products of $CaSO_4$ for 168 h at 871°C in a sealed, evacuated quartz capsule that also contained a specimen of Ni–23.5 Al–0.5 Hf–0.2 B, at. %, (IC-50).

This layer is shown at higher magnification in Fig. 26. Note the small spherical features; we assume that they represent the Ni-Ni_3S_2 eutectic composition.

The attack on Hastelloy X, must,, therefore, involve the rapid formation of a protective layer of Cr_2O_3 through which sulfur atoms diffuse slowly to the Cr_2O_3-metal interface, where they react to form Ni_3S_2 and other sulfides. The difference between Hastelloy X and the Ni_3Al-base alloys, is, thus, in a sense, more a matter of degree than of kind. The Cr_2O_3 layer on Hastelloy X is more resistant to sulfur penetration (either because it forms more quickly or because it is more compact) than the corresponding Al_2O_3 scale on Ni_3Al. One might well expect changes in the microstructure of the Al_2O_3 scale to result in improved resistance to sulfur penetration.

M-17054

Fig. 26. Higher magnification view of inner corrosion product layer on Hastelloy X specimen shown in Fig. 25.

CORROSION IN CIRCULATING LOOP TESTS

The environment in the circulating loop tests was much more benign (Table 8). At 871°C the equilibrium partial pressure of sulfur over $CaSO_4$ is about 10^{-19} Pa (10^{-24} atm), and the continual additions of oxygen to maintain an oxygen pressure of about 1 Pa (10^{-5} atm) both prevented the depletion of oxygen in the loop and reduced p_{S_2} to about 10^{-23} Pa (10^{-28} atm). (No attempt was made to determine whether thermodynamic equilibrium was achieved in the ambient gases in the loop, and the sulfur pressures cited above should be considered as maximum values.) This sulfur pressure is far below the decomposition pressure of either Ni_3S_2 or FeS, and under equilibrium conditions we would not expect sulfidation of the nickel aluminides or the iron sample. The attack on the aluminides was, indeed, limited to the formation of an oxide layer 0.2 to 0.4 μm thick, consisting mostly of Al_2O_3. The oxide surface was typically covered with a layer of platelets and whiskers, as shown in Fig. 27. The

Table 8. Corrosion of experimental nickel aluminides by SO_2 and O_2 in loop tests

[SO_2 derived from $CaSO_4$ at 871°C. O_2 added to give $p_{O_2} \approx 1$ Pa (10^{-5} atm)]

Temperature (°C)	Alloy	Weight change (g/cm^2)	Remarks
650	IC-10	4.12×10^{-5}	Black film
	IC-15	6.1	Blue film
	IC-40	−0.6	Light blue film
	IC-83	1.1	Light blue film
	LRO-79	19.2	Dark scale
	Iron	2700.0	Black and gray scale
750	IC-10	8.4×10^{-5}	Blue film
	IC-15	6.7	Blue film
	IC-40	3.0	Film spalled
	IC-83	16.0	Blue film
	LRO-79	65.5	Dark scale
	Iron	2800.0	Blue and gray scale
871	IC-10	-2.2×10^{-5}	Film spalled
	IC-15	19.7	Gray film
	IC-40	5.0	Dark spots on film
	IC-83	75.0	Dark green scale
	LRO-79	−522.0	Heavy spalled scale
	Iron	3000.0	Black heavy scale

iron, on the other hand, was not only heavily oxidized but also formed substantial quantities of FeS. The scale microstructure, which was observed at 650 and 750°C as well as at 871°C, is illustrated in cross section in Fig. 28(*a*). The S *Kα* x-ray image [Fig. 28(*b*)] of the scale-metal interface identifies the lighter areas in Fig. 28(*a*) as FeS. Note that filaments of FeS, perhaps in grain boundaries, extend all the way to the sulfide-gas interface.

This result is important because it demonstrates the existence of a mechanism for greatly increasing the activity of sulfur at the surface of an oxide scale. In order for sulfur to diffuse through an apparently compact layer of iron oxide, the sulfur pressure at the oxide-gas interface must exceed the decomposition pressure (~10^{-4} Pa at 871°C) of FeS. The specific mechanism involved has not yet been identified, but we suggest

ORNL-PHOTO 0266-84

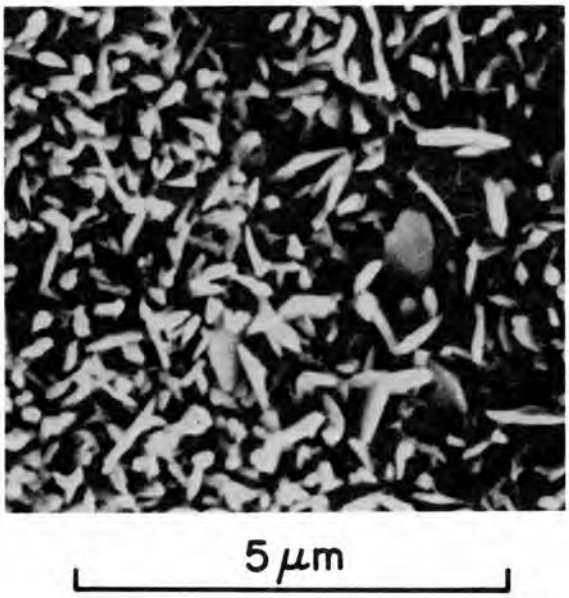

Fig. 27. Surface of Ni—24 Al—0.2 B, at. %, (IC-2) specimen exposed for 168 h at 871°C in a circulating loop in a mixture of oxygen at 1 Pa (10^{-5} atm) and the decomposition products of $CaSO_4$.

ORNL-PHOTO 0264-84

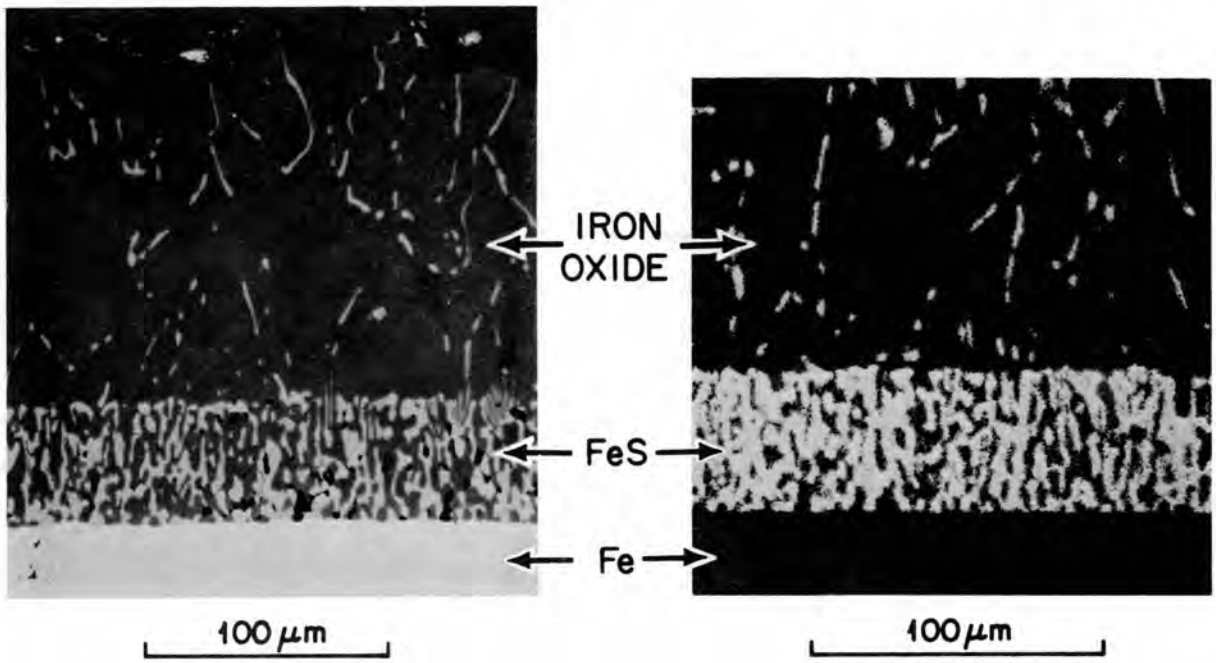

(*a*) (*b*)

Fig. 28. Iron specimen exposed 168 h at 871°C in a circulating loop in a mixture of oxygen at 1 Pa (10^{-5} atm) and the decomposition products of $CaSO_4$. (*a*) Bright field optical micrograph of scale cross section; (*b*) S *Kα* x-ray image of scale cross section.

that it involves the adsorption of SO_2 molecules on the oxide surface. The S-O bonds of an SO_2 molecule adsorbed on a rapidly growing oxide scale would be quickly broken and the oxygen incorporated in the oxide lattice, leaving an adsorbed sulfur atom on the oxide surface. If the sulfur desorption process is slow, the activity of sulfur at the oxide-gas interface would increase dramatically relative to its equilibrium value, ultimately reaching a point at which diffusion of sulfur into the oxide scale and the formation of FeS become possible. A rather similar mechanism has recently been proposed by Haflan and Kofstad[21] to explain the formation of NiO and Ni_3S_2 in a mixed-gas reaction where only $NiSO_4$ is thermodynamically stable. Whether this proposed mechanism is correct or not, the results of the loop tests do show that Ni_3Al-base alloys can resist sulfidation under conditions such that iron is heavily attacked.

Another unexpected result in the loop tests was the extent of spalling when the Ni—49 at. % Al and Ni—24 at. % Al—0.2 at. % B specimens were cooled to room temperature. This effect is shown in Figs. 29 and 30. Figure 29 is a scanning electron micrograph of the surface of an Ni—49 at. % Al specimen, and in Fig. 30 the scale on Ni—24 at. % Al—0.2 at. % B has been lifted off the specimen with a piece of tape and turned over so as to reveal the oxide-metal interface. The undulations in the film were caused by the bending of the tape, but the polishing marks from the specimen surface were reproduced.

As indicated in previous sections, air oxidation of boron-doped Ni_3Al caused only very slight spalling after 500 h at 1000°C and negligible spalling at 800°C. Oxidation of an electropolished sample at 1100°C in H_2-H_2O mixtures with $p_{O_2} \approx 10^{-13}$ Pa (10^{-18} atm) produced a thin but adherent Al_2O_3 scale. By contrast, as indicated above, the loop specimens spalled badly at 650, 750, and 871°C. Thus, possible variables influencing oxide spalling include oxygen pressure and the chemical nature of the environment. The air oxidation study has shown that spalling of oxide scales on aluminides can be eliminated by alloying with a small amount (<1 at. %) of hafnium.

M-19398

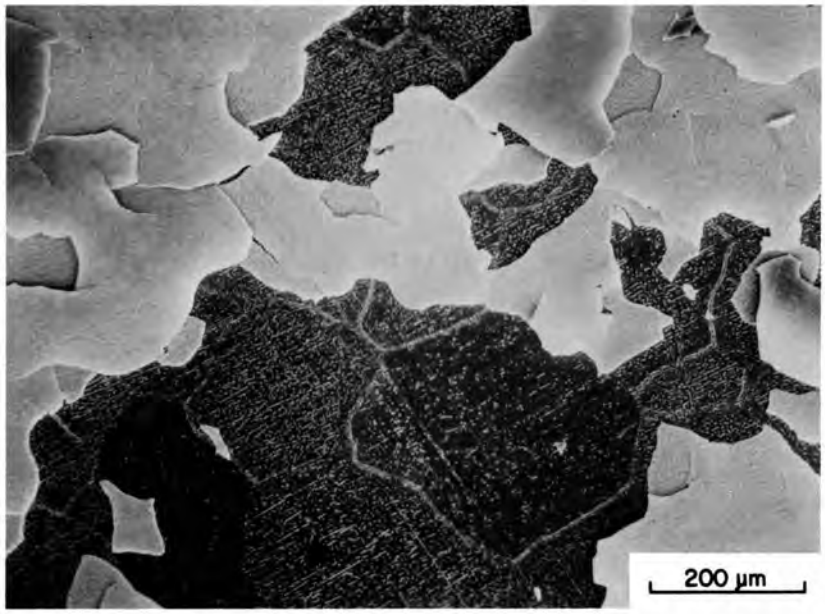

Fig. 29. Surface of a Ni—49 at. % Al specimen exposed for 168 h at 871°C in a circulating loop in a mixture of oxygen at 1 Pa (10^{-5} atm) and the decomposition products of $CaSO_4$.

M-19415

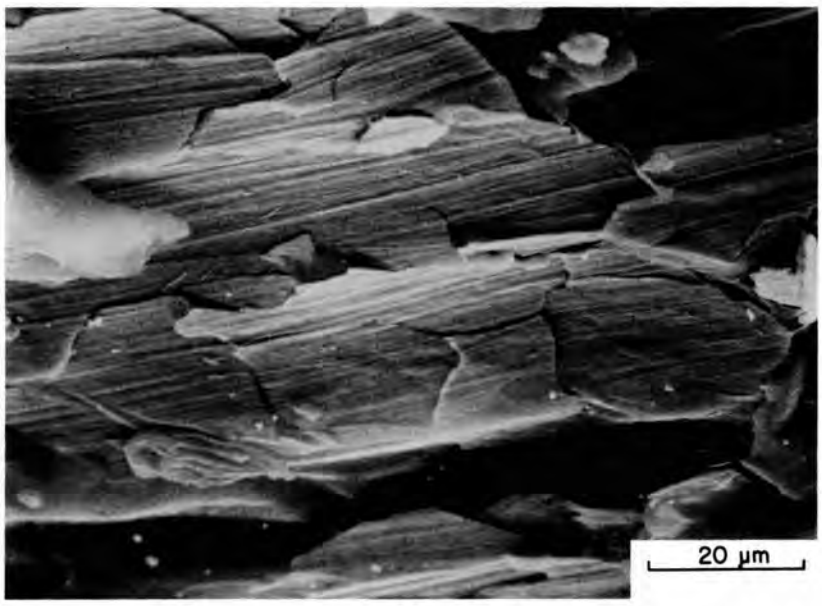

Fig. 30. The oxide-metal interface of the scale formed on a Ni—24 Al—0.2 B, at. %, (IC-2) specimen exposed for 168 h at 871°C in a circulating loop in a mixture of oxygen at 1 Pa (10^{-5} atm) and the decomposition products of $CaSO_4$.

WELDABILITY OF ALUMINIDES

An important area in the development of any commercial alloy is the ease with which it may be joined or welded. We investigated the weldability of the boron-doped ductile aluminides by gas tungsten arc (GTA) and electron beam welding processes.

Alloys investigated are listed in Table 9. Of principal interest were alloys IC-14 and IC-25 in the form of recrystallized sheets. We also studied a series of Ni_3Al alloys with varying amounts of boron to determine the effect of boron on weldability. Electron beam welds were made on 0.7-mm-thick sheets, and beam voltage and current were adjusted to produce full-penetration welds. A series of autogenous welds (i.e., without filler metal) was made with systematic variations in travel speed and beam focus. A Hamilton standard 6-kW electron beam welder was used in this study. The welding speed varied from 2 to 64 mm/s. The focus control number was varied 25 units above sharp focus on the sheet surface. Various sections of the welds were prepared for metallographic observation by standard techniques.

Table 9. Alloys selected for welding tests

Alloy	Content (wt %)					
	Al	Fe	Mn	Ti	B	Ni
IC-2	12.7					Balance
IC-6	12.7				0.1	Balance
IC-14	10.8	10.7	1.1	0.5	0.05	Balance
IC-15	12.7				0.05	Balance
IC-18	12.7				0.025	Balance
IC-19	12.7				0.01	Balance
IC-25	9.8	10.7	0.5	0.5	0.05	Balance

EFFECT OF OPERATING PARAMETERS

Initial gas tungsten arc welding (GTAW) of boron containing iron-nickel aluminide IC-25 produced severe cracking within the weld metal and

the heat-affected zone (HAZ). The different manifestations of cracking in welds are the following:

1. solidification cracking,
2. liquation cracking in the HAZ,
3. combination of the above two, and
4. elevated-temperature (subsolidus) cracking during heat treatment of welds.

Weld cracking due to the above factors has been the subject of several experimental studies.[22-25] In IC-25 the cracking appeared to nucleate in the HAZ and propagate into the fusion zone. A similar problem encountered in thorium-doped iridium alloys used in radioisotopic thermoelectric generators for space applications was attributed to the formation of liquation cracks in the HAZ and further propagation of these cracks into the fusion zone.[26] However, careful examination of the cracked surfaces in IC-25 revealed no evidence of liquation cracking. Also, the cracking problem in iridium alloys was in part due to the nature of the heat source available in the GTA process.[26] In iridium alloys the cracking problem was overcome by electron beam or laser welding processes with their highly concentrated heat source capability. The electron beam as a heat source can be controlled more precisely than can an electric arc. Hence, autogenous electron beam welding was mainly used on the ductile aluminides. Initial results for IC-25 are summarized in Fig. 31. Most of the welds showed a tendency to crack in the fusion zone and in the HAZ. However, some successful full-penetration welds were made at the lower welding speeds, and cracking severity was found to be a strong function of welding speed, as shown in Fig. 32. Cracking severity in this investigation is defined as the number of microcracks per unit length (mm) of the weld as observed on the weld surface. The cracking severity of the alloy increases dramatically at welding speeds greater than 12.7 mm/s (30 in./min).

EFFECT OF BORON

Problems related to weldability, in particular cracking, have traditionally been associated with unwanted difficult-to-eliminate tramp

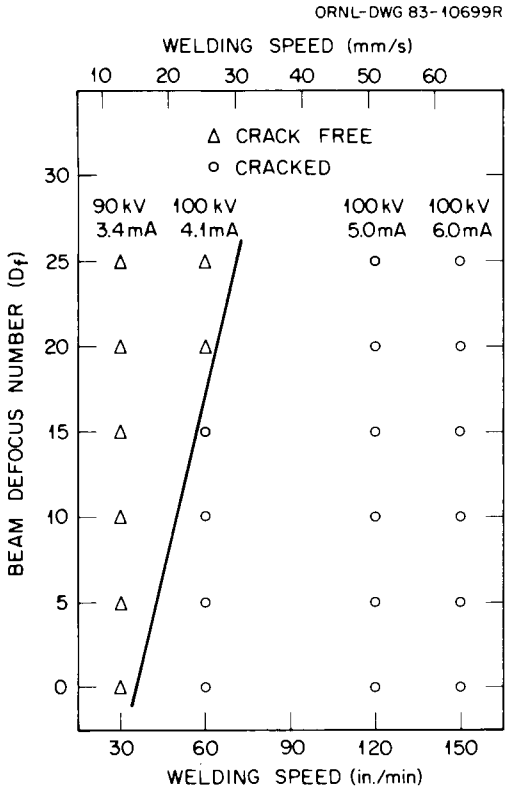

Fig. 31. Weldability of IC-25 as a function of welding speed and beam defocusing number.

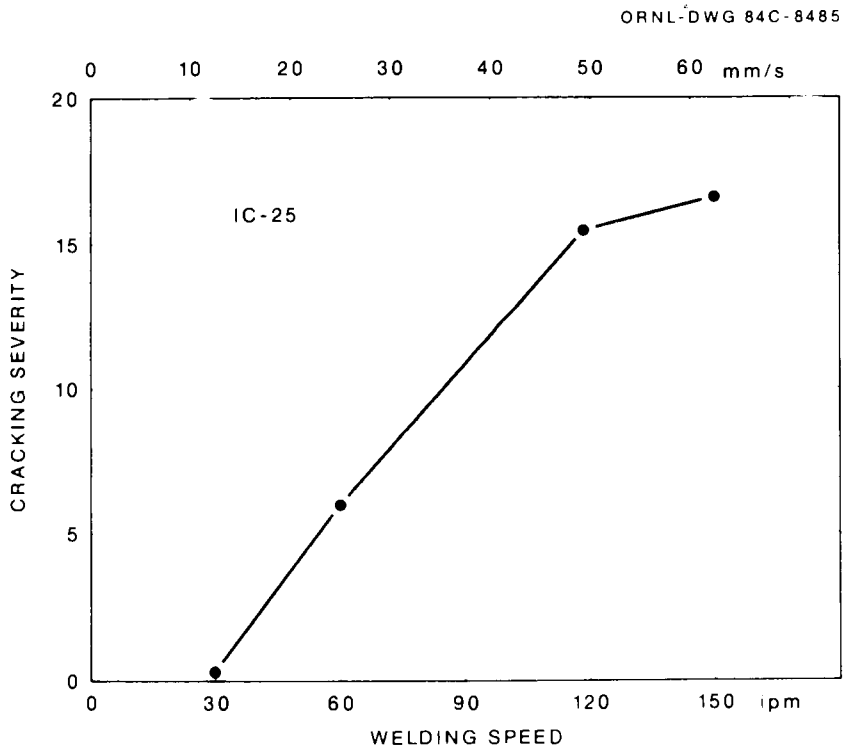

Fig. 32. Effect of welding speed on cracking severity of IC-25.

elements, such as phosphorus and sulfur, in both the base and filler metals. Also, intentional minor alloy additions affect weldability, as in the case of carbon and boron in nickel-base superalloys.[27] Although boron improves the ductility of polycrystalline Ni_3Al, it does not seem to improve the weldability to the same degree. A series of welds was made on Ni_3Al containing various boron contents (0 to 1000 wt ppm). The cracking severity of Ni_3Al as a function of boron content is shown in Fig. 33. The severity of cracking decreased dramatically with the additions of boron up to 200 ppm but increased with further additions of boron. The alloy containing no boron cracked the most. The cracking was predominantly in the HAZ. In superalloys, boron produces several beneficial effects, including improved elevated-temperature strength and improved ductility during fabrication, but boron has been found to contribute to the loss of hot ductility in the

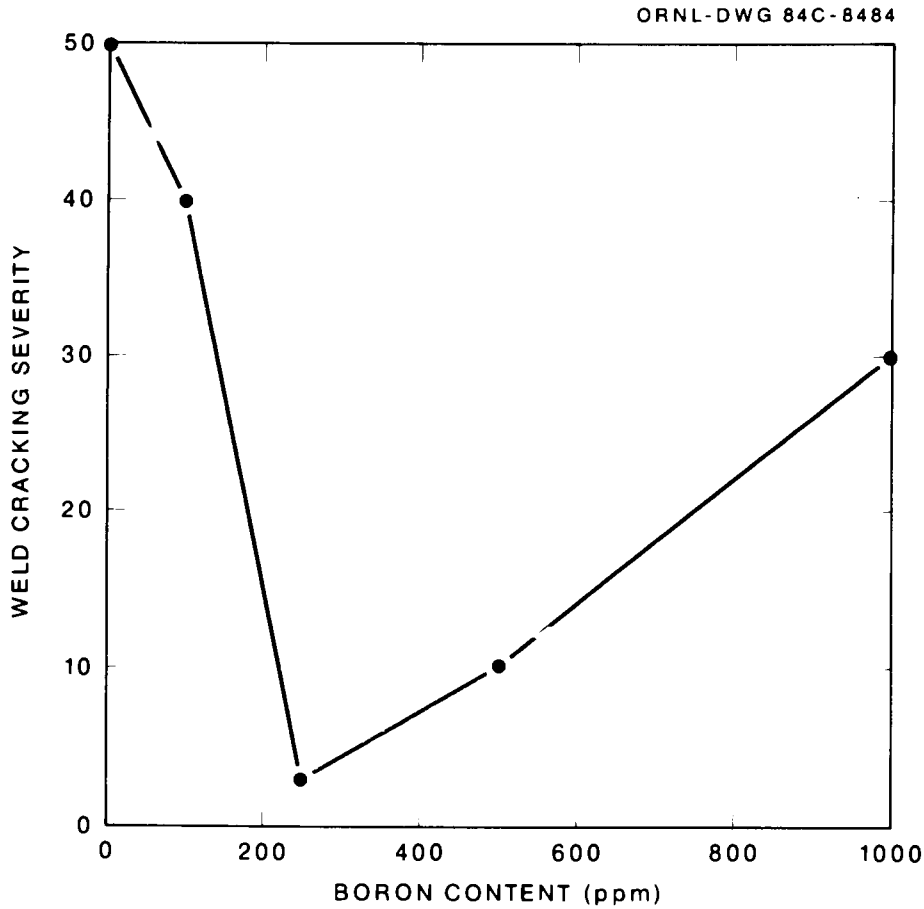

Fig. 33. Effect of boron content on weld cracking severity of IC-25.

HAZ (ref. 28). This has been related to localized melting and cracking in the HAZ of superalloys. Although boron has segregated preferentially to grain boundaries in boron-doped aluminides,[8] no evidence of localized melting was observed in the HAZ. However, a ductility minimum at elevated temperature associated with solute segregation that could lead to cracking is a possibility. The mechanisms that control hot cracking tendency in this alloy are not fully defined.

MICROSTRUCTURE

Microstructural features of both alloys IC-25 and IC-14 are very similar. Figure 34 shows cracking in the fusion zone and the HAZ of an IC-25 electron beam weld. The fusion zone contains predominantly a branched dendritic structure with a second phase in the interdendritic regions. Also significant precipitation occurs along the grain boundaries of the HAZ during the weld thermal cycle (Fig. 35). This phase has been identified as martensitic β' phase (Fig. 36) by TEM. The origin of the

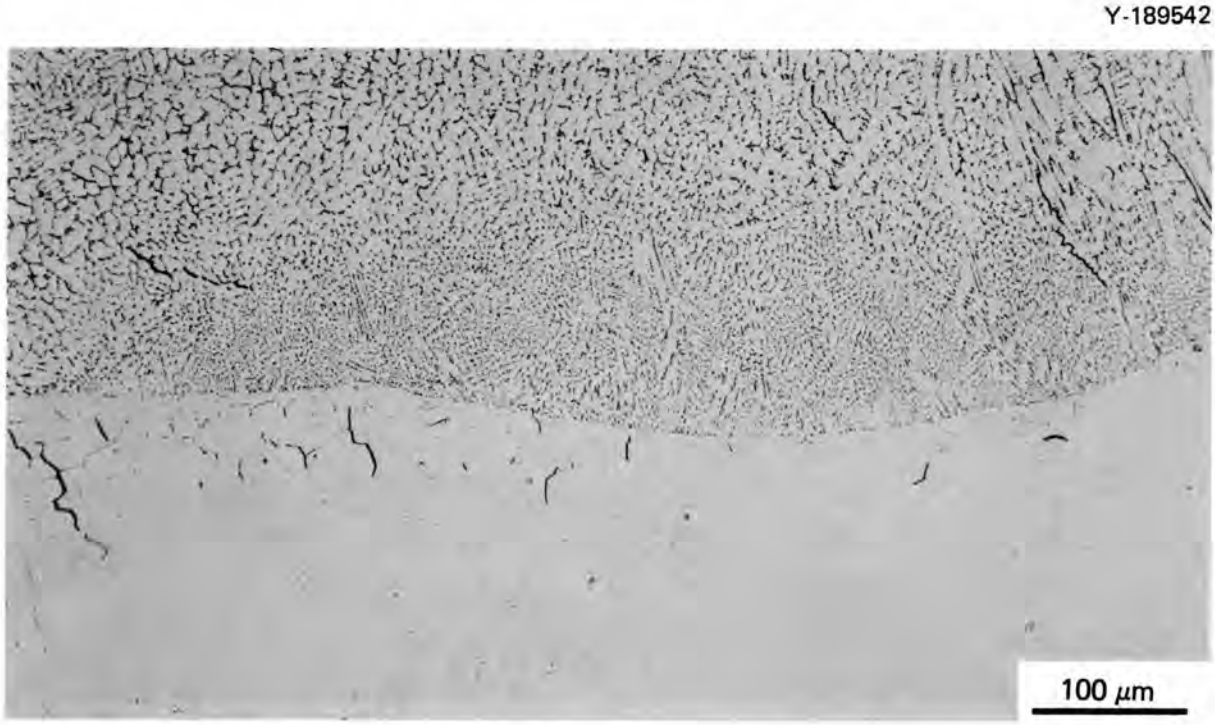

Fig. 34. Optical microstructure of electron beam weld on IC-25 showing crack formation in the fusion zone and HAZ.

Y-189527

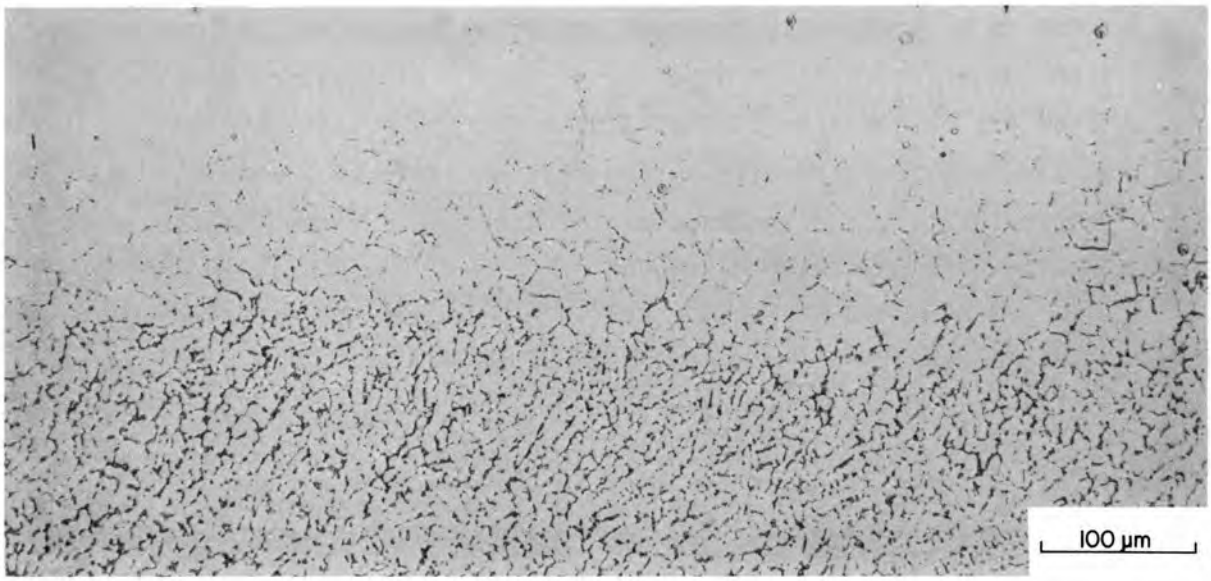

Fig. 35. Electron beam weld on IC-25 showing precipitation of β′ phase on grain boundaries in the HAZ.

ORNL-PHOTO 4963-83

Fig. 36. Transmission electron micrograph of IC-25 weld showing the morphology of martensitic β′ particles.

martensitic β' phase in the microstructure is related to the weld thermal cycle. In the fusion zone, aluminum enrichment of the interdendritic liquid during solidification leads to the formation of β', and subsequent transformation of β' to a martensitic phase is due to the rapid cooling encountered during welding. However, in the HAZ, where the specimen is subjected to peak temperatures above the peritectoid temperature, β' will precipitate as predicted by the phase diagram, leading to a duplex $\gamma + \beta'$ structure. In both the fusion zone and the HAZ, the presence of martensitic β' represents a nonequilibrium situation resulting from the weld thermal cycle. After the weld specimen is homogenized at 1000°C for 5 h, the β' phase goes into solution, as shown in Fig. 37.

SUMMARY AND FUTURE WORK

New improved alloys are needed for hot components in severe environments for applications in advanced coal conversion and utilization systems, advanced heat engines, and high-temperature heat recovery systems. The objective of this study is to develop new high-temperature structural materials based on nickel and nickel-iron aluminides. The initial development has been focused on the Ni_3Al system with iron additions.

Nickel-iron aluminides based on Ni_3Al can be ductilized by adding a few hundred parts per million of boron. The study of phase relationships indicates that iron atoms occupy both nickel and aluminum sublattice sites available in the ordered fcc Ni_3Al crystal structure ($L1_2$-type). The aluminide can dissolve less than 15 at. % Fe. Beyond the solubility limit, formation of a martensitic β' phase (a transformed $B2$ phase) and of a cellular structure (webs of disordered γ material surrounding ordered γ' regions) was observed in the aluminides containing 15 and 20 at. % Fe. The stability of these phases is sensitive to the aluminum-to-nickel ratio, in agreement with the ternary phase diagram of Ni-Al-Fe constructed by Rivlin and Raynor.[15]

Mechanical properties of selected nickel-iron aluminides were characterized by tensile tests as a function of temperature. Iron additions harden Ni_3Al effectively at temperatures to 850°C. The yield strength of

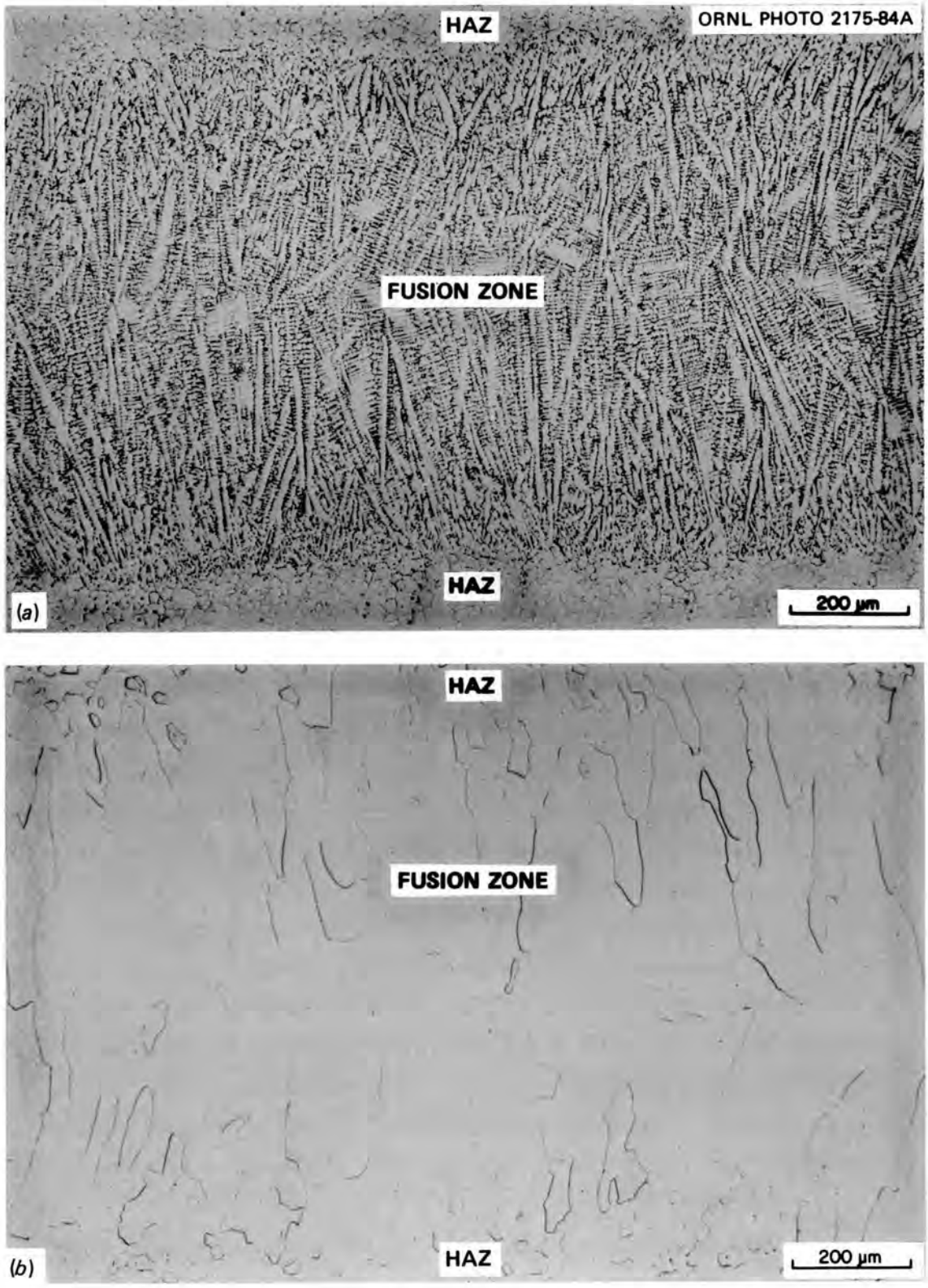

Fig. 37. Optical microstructure of electron beam weld on IC-25. (*a*) As-welded fusion zone. (*b*) Fusion zone after heat treatment of 5 h at 1000°C.

the nickel-iron aluminides increases with test temperature and reaches a maximum around 650°C. As a result of this increase, the aluminides are much stronger than wrought commercial superalloys at elevated temperatures.

The base compositions of nickel-iron aluminides were further modified with alloy additions, including Hf, Zr, Ti, Ta, Nb, Cr, and Mn. Among these elements, hafnium is most effective in improving the mechanical and metallurgical properties of the base aluminides. Surprisingly, hafnium strengthens the aluminides more effectively at elevated temperature than at room temperature. This observation suggests that hafnium in solid solution promotes the thermally activated cross-slip mechanism by changes in the anti-phase boundary and stacking fault energies. The aluminide modified with 1.5 at. % Hf exhibits a yield strength of 923 MPa (134,000 psi) at 850°C, which is higher than that of commercial superalloys, including cast superalloys.

The nickel-iron aluminides exhibit good tensile ductility (>30%) at room temperature. Their ductility generally decreases with increasing temperature and reaches a low value below 15% at 1000°C. The fracture mode changes from transgranular to intergranular as the ductility decreases.

Generally, Ni_3Al showed slight spalling during cyclic oxidation at 1000°C. The spalling can be inhibited by alloying with a small amount of hafnium, which improves the adhesion between base metal and oxide scale. The hafnium-modified nickel aluminides have the best oxidation resistance. Their oxidation rates are lower than those of Hastelloy X and type 316 stainless steel by factors of 2 and 200 at 1000°C, respectively. The superior oxidation resistance of these aluminides comes from the formation of compact and adherent films of aluminum oxides in oxidizing environments.

Two types of apparatus were used to study the corrosion behavior of nickel-iron aluminides in sulfidizing-oxidizing environments. The first consists of an evacuated quartz tube containing $CaSO_4$ and a test specimen either embedded in the $CaSO_4$ or suspended in the vapor phase above it. The other apparatus is a closed circulating loop in which helium passes over a heated bed of $CaSO_4$ decomposition products, which then react with specimens suspended in the loop. The p_{S_2}/p_{O_2} ratio can be varied through additions of O_2 or SO_2 to the carrier gas. Test temperatures range from 650 to 871°C.

Capsule tests have demonstrated the vulnerability of high-nickel alloys to attack by the decomposition products of $CaSO_4$ under conditions where, in a closed system, oxygen depletion may occur. However, the tests also showed that at least in certain temperature ranges an oxide scale can be formed on nickel aluminides and provide protection against sulfidation. The loop tests indicate that sulfur attack can be entirely suppressed by an increase in the oxygen activity in the ambient gas. Special capsule tests also showed that the accelerated oxidation-sulfidation corrosion observed in coal combustion environments using limestone to control SO_2 emissions could be caused not only by the $CaSO_4$ deposit itself, as previously suggested, but also by the decomposition products (SO_2 and O_2) of $CaSO_4$. The combined results from capsule and closed-loop tests showed the dependence of sulfidation on oxygen partial pressure and verified that the severe corrosion of nickel aluminides in capsule tests was caused by oxygen depletion in a closed system.

The ductile aluminides are prone to cracking during welding. However, these aluminides can be electron beam welded successfully under closely controlled conditions. Boron content and welding speed affect the weldability of the aluminides. Although boron improves the ductility of polycrystalline aluminides, it does not seem to improve the weldability to the same degree.

The observed hot cracking in the HAZ and the fusion zone during welding of the aluminides was predominantly intergranular. Although the weld cracking observed in this class of materials appears to be similar to that in the nickel-base superalloys containing boron, no localized melting was observed. The hot cracking mechanism in this alloy system is not fully defined.

The weld metal microstructure was duplex, with about 9 to 12 vol % second phase identified as martensitic β' precipitate, and subsequent transformation to martensitic phase occurred along the grain boundaries in the HAZ. This second phase may be eliminated from the weldment by suitable postweld heat treatment.

The work on the basic alloy development will continue and focus on several areas. Mechanical properties in addition to tensile properties

will be determined. These include creep resistance, fatigue properties, and crack growth behavior. Initial results of creep tests indicate that hafnium additions substantially improve the creep resistance of nickel-iron aluminides. Fatigue resistance will be characterized under both strain- and load-controlled conditions.

The aluminides generally show a decrease in ductility with increasing test temperature. The ductility of some aluminides dropped to a rather low level at 1000°C. Future studies will be aimed at improving the high-temperature ductility, with emphasis on hot fabricability of the aluminides. Large heats of selected aluminides will be prepared by industrial processes. The properties of these large heats will be compared with those of laboratory heats and of commercial heat-resistant alloys. Formability and fabricability of the aluminides will also be demonstrated.

The aluminide development will extend from the current Ni_3Al-Fe_3Al system to the NiAl-FeAl system. The latter system is of interest because it contains 50 at. % Al and is thus expected to have better corrosion resistance in sulfidizing environments. In addition, NiAl-FeAl aluminides have lower density and better high-temperature capabilities because of their higher melting points.

Capsule tests will continue because they have proved to be a simple and convenient method for the screening of large numbers of alloys to be tested and for the determination of the effect of various surface conditions on the corrosion resistance in sulfidizing environments. Although it is difficult to define precisely the test conditions inside the capsule, the ability of an alloy to survive a capsule test is prima facie evidence that the oxide scale on the alloy is highly protective and is resistant to sulfur penetration. Thus, these tests provide a convenient measure of the role of oxide microstructure in limiting the attack of alloys in corrosive environments.

On the other hand, the capsule tests cannot define the corrosion environment because the p_{O_2} and p_{S_2} are uncontrolled. Because an understanding of the corrosion mechanism and alloying effects may require such control, closed-loop tests will also be run under conditions such that both the p_{S_2} and p_{O_2} are controlled by fixing predetermined pressures of SO_2, CO_2, and CO.

Work on the welding of ductile aluminide sheet materials will continue on two fronts. Electron beam welding techniques and procedures will continue to be refined and will involve such things as reducing welding speeds and tapering the beam current at weld termination to minimize crater cracking. Preheating to moderate temperatures (several hundred degrees Celsius) before welding may present a way to eliminate cracking too, and preparations are now being made to examine this. Also, some welding with other processes, such as GTAW, will begin.

Besides investigating weldability from a practical point of view, efforts aimed at understanding welding-related cracking in the ductile aluminides are in progress. Gleeble testing will begin, which involves simultaneous application of a simulated weld thermal cycle and a controlled strain to a specimen. In some cases the Gleeble techniques have been instrumental in identifying cracking mechanisms in conventional alloys. A subsize specimen shape and testing procedure will be developed for ductile aluminide sheet, and a thermal cycle measured in the HAZ of an electron beam weld on 0.76-mm sheet will be programmed into the Gleeble control system.

It is anticipated that Gleeble testing will provide a means for better understanding the role of microstructure in weld cracking susceptibility and help identify and neutralize cracking mechanisms in the ductile aluminide alloys.

ACKNOWLEDGMENTS

The authors gratefully acknowledge the significant program management of R. A. Bradley, A. C. Schaffhauser, J. A. Carpenter, Jr., and R. R. Judkins. They wish to thank J. O. Stiegler for helpful discussions. Thanks are also due to E. H. Lee and M. Winsbro for technical assistance, R. S. Crouse for scanning electron microscopy, W. H. Farmer for metallography, L. Queener and R. L. Heestand for melting and casting, Sigfred Peterson for technical editing, Connie Dowker and Lou Pyatt for typing the draft and D. L. LeComte for preparation of the final manuscript.

REFERENCES

1. N. S. Stoloff and R. G. Davis, "The Mechanical Properties of Ordered Alloys," *Prog. Mater. Sci.* 13(1), 1–34 (1966).

2. B. H. Kear et al., *Ordered Alloys — Structural Applications and Physical Metallurgy*, Claitor's Publishing Division, Baton Rouge, La., 1970.

3. H. Warlimont, ed., *Ordered-Disorder Transformation in Alloys*, Springer-Verlag, New York, 1974.

4. J. H. Westbrook, "Intermetallic Compounds: Their Past and Promise," *Metall. Trans. A* 8A, 1327–60 (1977).

5. C. T. Liu and H. Inouye, "Control of Ordered Crystal Structure and Ductility of $(Fe,Co,Ni)_3V$ Alloys," *Metall. Trans. A* 10A, 1515–25 (1979).

6. C. T. Liu, "Physical Metallurgy and Mechanical Properties of Ductile Ordered Alloys $(Fe,Co,Ni)_3V$," *Int. Met. Rev.*, in press.

7. C. T. Liu and C. C. Koch, "Development of Ductile Polycrystalline Ni_3Al for High Temperature Applications," pp. P42-1–19 in *Technical Aspects of Critical Materials Use by the Steel Industry*, vol. IIB, Proceedings of a Public Workshop; "Trends in Critical Materials Requirements for Steels of the Future; Conservation and Substitution Technology for Chromium," Nashville, Tenn., Oct. 4–7, 1982, NBSIR 83-2679-2, National Bureau of Standards, June 1983.

8. C. T. Liu et al., "Preparation of Ductile Nickel Aluminides for High Temperature Use," pp. 32–41 in *Proceedings of the Symposium on High Temperature Materials Chemistry — II*, held in San Francisco on May 8–13, 1983, ed. Z. A. Munir and D. Cubicciotti, proc. vol. 83–7, The Electrochemical Society, Pennington, N.J., 1983.

9. K. Aoki and O. Izumi, "Improvement in Room Temperature Ductility of the $L1_2$ Type Intermetallic Compound Ni_3Al by Boron Addition," *Nippon Kinzoku Gakkaishi* 43, 1190–95 (1979).

10. E. M. Grala, "Investigations of NiAl and Ni_3Al," pp. 468–404 in *Mechanical Properties of Intermetallic Compounds*, ed. H. J. Westbrook, Wiley, New York, 1960.

11. W. C. Johnson et al., "Confirmation of Sulfur Embrittlement in Nickel Alloys," *Scr. Metall.* **8**, 971–74 (1974).

12. C. C. Koch et al., "Rapid Solidification Studies of Ni_3Al Alloys" presented at the Third International Conference on Rapid Solidification Processing, Gaithersburg, Md., Dec. 6–8, 1982.

13. R. W. Guard and J. H. Westbrook, "Alloying Behavior of Ni_3Al (γ' Phase), *Trans. AIME* 215, 807–14 (1959).

14. S. Ochiai et al., "Alloy Behavior of Ni_3Al, Ni_3Ga, Ni_3Si, and Ni_3Ge," *Acta Metall.* **32**, 289–98 (1984).

15. V. G. Rivlin and G. V. Raynor, "Critical Evaluation of Constitution of Aluminum-Iron-Silicon System," *Int. Met. Rev.* **26**, 133–52 (1981).

16. S. Takuchi and E. Kuramoto, "Temperature and Orientation Dependence of the Yield Stress in Ni_3Ga Single Crystals," *Acta Metall.* **21**, 415–27 (1973).

17. R. G. Davis and N. S. Stoloff, "On the Yield Stress of Aged Ni-Al Alloys," *Trans. AIME* **233**, 714–19 (1965).

18. C. Lall, S. Chin, and D. P. Pope, "The Orientation and Temperature Dependence of the Yield Stress of $Ni_3(Al,Nb)$ Single Crystals," *Metall. Trans. A* 10A, 1323–32 (1979).

19. J. Stringer et al., "In Bed Corrosion of Alloys in Atmospheric Fluidized Bed Combustor," pp. 433–41 in *Fluidized Bed Combustion*, Vol. 8, U.S. Department of Energy, Washington, D.C., 1980.

20. P. J. Ficalora, *Hot Corrosion Reactions of Calcium Sulfate with Cr, Ni, Co, Fe, and Several Alloys*, ORNL/TM-8735, June 1983.

21. B. Haflan and P. Kofstad, "The Reaction of Nickel with $SO_2 + O_2/SO_3$ at 500–900°C," *Corros. Sci.* 23, 1333–52 (1983).

22. P. P. Puzak, W. R. Apblett, and W. S. Pellini, "Hot Cracking of Stainless Steel Weldments," *Weld. J. (New York)* 35(1), 96–175-s (1956).

23. W. R. Apblett and W. S. Pellini, "Factors Which Influence Weld Hot Cracking," *Weld. J. (New York)* 35(1), 83–90-s (1956).

24. J. C. Borland, "Generalized Theory of Super-Solidus Cracking in Welds (and Castings)," *Br. Weld. J.* 7, 558–59 (1960).

25. F. C. Hull, "Effect of Delta Ferrite on the Hot Cracking of Stainless Steel," *Weld. J. (New York)* 46(8), 399–409-s (1967).

26. S. A. David and C. T. Liu, "Weldability and Hot Cracking in Thorium-Doped Iridium Alloys," *Met. Technol. (London)* 7, 102–6 (March 1980).

27. W. A. Owcszrski, "Some Minor Element Effects on Weldability of Heat Resistant Nickel-Base Alloys," pp. 6–23 in *Effects of Minor Elements on the Weldability of High-Nickel Alloys*, Welding Research Council, New York, 1969.

28. W. A. Owczarski, D. S. DuVall, and C. P. Sullivan, "A Model for Heat-Affected Zone Cracking in Nickel-Base Superalloys," *Weld. J. (New York)* 45(4), 145–53-s (1966).

ORNL-6067

INTERNAL DISTRIBUTION

1–2. Central Research Library
3. Document Reference Section
4–5. Laboratory Records Department
6. Laboratory Records, ORNL RC
7. ORNL Patent Section
8. P. F. Becher
9. J. Bentley
10–14. R. A. Bradley
15. R. S. Carlsmith
16 P. T. Carlson
17. J. A. Carpenter, Jr.
18–22. J. V. Cathcart
23. O. B. Cavin
24. G. W. Clark
25 G. L. Copeland
26. R. S. Crouse
27. A. DasGupta
28–32. S. A. David
33. J. H. DeVan
34. C. K. H. DuBose
35. J. S. Faulkner
36. B. E. Foster
37. W. R. Gambill
38. G. M. Goodwin
39. M. P. Guthrie
40. J. P. Hammond
41–45. J. A. Horton
46. L. L. Horton
47. G. E. Ice
48–52. H. Inouye
53. M. A. Janney
54–58. W. A. Jemian
59. R. R. Judkins
60. W. J. Lackey
61. E. H. Lee
62. B. C. Leslie
63–72. C. T. Liu
73. A. P. Maclin
74. L. K. Mansur
75. J. F. Martin
76. R. W. McClung
77. H. E. McCoy
78. D. L. McElroy
79. C. J. McHargue
80. C. G. McKamey
81. L. E. McNeese
82. T. K. Miller
83. A. J. Moorhead
84. A. R. Olsen
85. P. Patriarca
86. R. E. Pawel
87. P. R. Rittenhouse
88. T. K. Roche
89–93. M. L. Santella
94. A. C. Schaffhauser
95. J. H. Schneibel
96. G. M. Slaughter
97. C. J. Sparks, Jr.
98. J. O. Stiegler
99. D. P. Stinton
100. R. W. Swindeman
101. V. J. Tennery
102–104. P. T. Thornton
105. T. N. Tiegs
106. P. F. Tortorelli
107. J. R. Weir
108. F. W. Wiffen
109. R. O. Williams
110. H. L. Yakel
111. R. J. Charles (Consultant)
112. Alan Lawley (Consultant)
113. T. B. Massalski (Consultant)
114. R. H. Redwine (Consultant)
115. J. C. Williams (Consultant)
116. K. M. Zwilsky (Consultant)

EXTERNAL DISTRIBUTION

117. ALUMINUM COMPANY OF AMERICA LABORATORIES, Alcoa Technical Center, Route 780, Seventh Street Road, Alcoa Center, Pennsylvania 15269

G. MacZura

118. COLUMBIA UNIVERSITY, 1137 S.W. Mudd Building, New York, NY 10027

J. K. Tien

119. COMMISSION OF THE EUROPEAN COMMUNITIES, Petten Establishment, Postbus 2, 1755 ZG Petten, The Netherlands

Marcel Van de Voorde

120–123. ELECTRIC POWER RESEARCH INSTITUTE, 3412 Hillview Avenue, P.O. Box 10412, Palo Alto, CA 94303

W. T. Bakker
D. J. Frey
R. I. Jaffee
J. Stringer

124. GENERAL ELECTRIC COMPANY, Quartz and Chemicals Dept., 24400 Highland Road, Richmond Heights, OH 44413

G. W. Weber

125. INSTITUTE OF DEFENSE ANALYSES, 1801 Beauregard Street, Alexandria, VA 22311

T. F. Kearns

126. LEHIGH UNVERSITY, Materials Research Center, Bethlehem, PA 18015

Y. T. Chou

127. LOCKHEED CORPORATION, Palo Alto Laboratories, 3251 Hanover St., Palo Alto, CA 94304

E. C. Burke

128. MASSACHUSETTS INSTITUTE OF TECHNOLOGY, 77 Massachusetts Avenue, Room 13-5026, Cambridge, MA 02139

M. B. Bever

129. MONSANTO COMPANY, P.O. Box 1311, Texas City, TX 77590

P. S. Gupton

130. NORTH CAROLINA STATE UNIVERSITY, Materials Engineering Dept., Raleigh, NC 27650

C. C. Koch

131. RENSSELAER POLYMER INSTITUTE, Materials Engineering Dept., Troy, NY 12181

N. S. Stoloff

132. UNIVERSITY OF MASSACHUSETTS, Department of Polymer Science, Room 701, GRC, Amherst, MA 01003

R. S. Porter

133. VANDERBILT UNIVERSITY, Station B, P.O. Box 1621 Nashville, TN 37235

J. J. Wert

134. VIRGINIA POLYTECHNIC INSTITUTE AND STATE UNIVERSITY, Blacksburg, VA 24061

D. A. Farkas

135–136. DOE, ENERGY SYSTEMS RESEARCH AND DEVELOPMENT, Office of Conservation and Renewable Energy, Forrestal Building Independence Avenue, Washington, DC 20585

J. J. Brogan
J. J. Eberhardt

137–139. DOE, MORGANTOWN ENERGY TECHNOLOGY CENTER, P.O. Box 880, Morgantown, WV 26505

J. M. Hobday
J. E. Scholes
J. S. Wilson

140–143. DOE, PITTSBURGH ENERGY TECHNOLOGY CENTER, P.O. Box 10940, Pittsburgh, Pennsylvania 15236

R. A. Carabetta
S. W. Chun
A. W. Deurbrouch
S. R. Lee

144–145. DOE, OAK RIDGE OPERATIONS OFFICE, P.O. Box E, Oak Ridge, TN 37831

Office of Assistant Manager for Energy Research and Development
S. J. Wolf

146. DOE, OFFICE OF BASIC ENERGY SCIENCES, Materials Sciences Division, Washington, DC 20545

F. V. Nolfi, Jr.

147–153. DOE, OFFICE OF FOSSIL ENERGY, Washington, DC 20545

J. P. Carr
S. J. Dapkunas
C. Garrett
R. E. Harrington
L. Naphtali
P. Scott
T. B. Simpson

154. DOE, OFFICE OF VEHICLE AND ENGINE R&D, Route Symbol CE-131, Forrestal Building, Washington, DC 20585

R. B. Schulz

155–181. DOE, TECHNICAL INFORMATION CENTER, Office of Information Services, P.O. Box 62, Oak Ridge, TN 37831